Key Points:
- We propose a new phase field approach for fluid-driven fracturing in elastic media
- The approach fully couples the elastic deformation of the medium, fracture apertures, and fluid flow inside the fractures
- We find excellent agreement between the proposed model and analytical solutions of fracture propagation

Correspondence to:
D. Santillán,
david.santillan@upm.es

This article was corrected on 19 MAY 2017. See the end of the full text for details.

Phase field model of fluid-driven fracture in elastic media: Immersed-fracture formulation and validation with analytical solutions

David Santillán[1] (iD), **Ruben Juanes[2,3]** (iD), **and Luis Cueto-Felgueroso[1,2]**

[1]Department of Civil Engineering: Hydraulics, Energy and Environment, Technical University of Madrid, Madrid, Spain, [2]Department of Civil and Environmental Engineering, Massachusetts Institute of Technology, Cambridge, Massachusetts, USA, [3]Department of Earth, Atmospheric and Planetary Sciences, Massachusetts Institute of Technology, Cambridge, Massachusetts, USA

Abstract Propagation of fluid-driven fractures plays an important role in natural and engineering processes, including transport of magma in the lithosphere, geologic sequestration of carbon dioxide, and oil and gas recovery from low-permeability formations, among many others. The simulation of fracture propagation poses a computational challenge as a result of the complex physics of fracture and the need to capture disparate length scales. Phase field models represent fractures as a diffuse interface and enjoy the advantage that fracture nucleation, propagation, branching, or twisting can be simulated without ad hoc computational strategies like remeshing or local enrichment of the solution space. Here we propose a new quasi-static phase field formulation for modeling fluid-driven fracturing in elastic media at small strains. The approach fully couples the fluid flow in the fracture (described via the Reynolds lubrication approximation) and the deformation of the surrounding medium. The flow is solved on a lower dimensionality mesh immersed in the elastic medium. This approach leads to accurate coupling of both physics. We assessed the performance of the model extensively by comparing results for the evolution of fracture length, aperture, and fracture fluid pressure against analytical solutions under different fracture propagation regimes. The excellent performance of the numerical model in all regimes builds confidence in the applicability of phase field approaches to simulate fluid-driven fracture.

1. Introduction

Fluid-driven fracturing plays an important role in natural and engineering processes. Some examples are the transport of magma in the lithosphere [*Spence and Turcotte*, 1985; *Rubin*, 1995; *Parmigiani et al.*, 2016], the geologic sequestration of carbon dioxide [*Cappa and Rutqvist*, 2011; *Jha and Juanes*, 2014], the preconditioning in rock masses to control the timing of goaf events [*Jeffrey and Mills*, 2000], the creation of chemically reactive barriers to inhibit the contaminant migration in the vadose zone [*Murdoch*, 2002], the stimulation of geothermal reservoirs to increase heat extraction [*Legarth et al.*, 2005; *Evans et al.*, 2005], or the enhanced oil and gas recovery from unconventional low-permeability reservoirs [*Economides and Nolte*, 2000; *Patzek et al.*, 2013; *Cueto-Felgueroso and Juanes*, 2013], among many others. Since technically recoverable gas resources worldwide from unconventional reservoirs are estimated at approximately 8000 trillion cubic feet [*Kuuskraa et al.*, 2013], the last engineering application has a growing interest which stems from the environmental stewardship. The created fractures may unintentionally provide access between the reservoir and the surrounding environment, leading to leakage of fracturing fluid or gas with the potential of groundwater contamination [*Osborn et al.*, 2011; *Vidic et al.*, 2013]. Both perspectives of the engineering and environmental concerns require rigorous mathematical models and numerical simulation tools capable of reproducing the complex physics involved in the process of hydraulic fracturing.

Fluid-driven fracture propagation in elastic media can be simulated through analytical solutions for simple fracture geometries and injection protocols. The most widely used are the Khristianovic-Geertsma-de Klerk (KGD) model, which assumes plane strain conditions [*Geertsma and De Klerk*, 1969; *Khristianovich and Zheltov*, 1955], the Perkins-Kern-Nordgren model, which considers an elliptic-shaped cross-section fracture of constant height under plane strain deformation [*Perkins and Kern*, 1961; *Nordgren*, 1972], and the penny-shaped or

radial model, where the fracture propagates symmetrically with respect to the injection well and perpendicular to it. Most analytical formulations are solved in an infinite linear elastic domain, where an incompressible Newtonian fluid is injected at constant volumetric rate. *Detournay* [2016] gives an overview and current state of the art of analytical solutions for the asymptotic behavior of the tip region and the propagation of a penny-shaped fracture for a constant injection rate.

The propagation of a plane strain fluid-driven fracture in an impermeable elastic medium is controlled by the competition between two dissipation processes: the viscous dissipation due to flow of the fluid in the fracture and the toughness dissipation due to fracturing of the medium [*Detournay*, 2004]. The relative importance of these dissipation processes leads to two limiting propagation regimes, namely, the viscous-dominated regime, whose analytical solutions are provided in *Adachi and Detournay* [2002] and *Garagash and Detournay* [2005], and the toughness-dominated regime, whose solution is given in *Garagash* [2006]. If the medium is permeable, the storage of fluid must also be considered, and two new scenarios arise: the fluid may be mostly concentrated in the porous medium — leak-off regime — or in the fracture — storage regime [*Hu and Garagash*, 2010]. Analytical solutions with leak off (which assume that the fluid in the medium does not affect the deformation field) exist for the toughness-dominated regime [*Bunger et al.*, 2005] and for the viscous-dominated regime [*Adachi and Detournay*, 2008], among many others available in the literature.

Numerical models of fracture can be classified into two categories: discrete and continuum approaches. The discrete approach simulates fractures as discontinuities. From a numerical point of view, fractures are propagated by splitting nodes [*Fu et al.*, 2013] or breaking elements [*Wangen*, 2011] in the case of finite element models or by splitting nodes and reconnecting springs in the case of spring network models [*Hafver et al.*, 2014]. Two drawbacks of these approaches are that the discretization must change topology due to fracture growth and that the fracture propagation is restricted to follow mesh lines. These disadvantages are overcome by either remeshing techniques [*Bouchard et al.*, 2003] or using advances approaches, such as the cohesive zone modeling [*Carrier and Granet*, 2012] or the enriching displacement method [*Oliver et al.*, 2006]. Other approaches are those based on the boundary element method [*Rungamornrat et al.*, 2005]. They are computationally efficient since the solutions are only solved on the boundaries and the fracture surfaces. The magnitude and direction of fracture propagation are governed by growth laws related to local stress intensity factors. The main disadvantages of this method are the difficulties in handling nonlinear or heterogeneous materials, or topological changes in the fracture trajectories such as joining or branching.

On the other hand, continuous approaches consider the intact and fractured areas as a whole, without the need of introducing discontinuities. Examples of continuous models include peridynamics, gradient damage models, or phase field models. Peridynamics is a nonlocal theory in which the solid is assumed to be composed of material points. Each point interacts with all its neighbors within a nonlocal region called *horizon* [*Ouchi et al.*, 2015]. Gradient damage models and phase field models exhibit many similarities although differences arise in the treatment of the strain localization procedure or the length scale over which damage spreads [*Shojaei et al.*, 2014]. In phase field models, fractures are described by incorporating a continuum field variable — the phase field — which interpolates between the broken and unbroken regions. The change from intact to broken regions takes place along a transition band of width controlled by parameters. The main advantages of this approach are that (i) all the method calculations are conducted on the initial undeformed topology; (ii) the method has the ability to simulate complex fracturing processes, such as branching, joining, propagation or nucleation, without the need for additional criteria; and (iii) heterogeneous media are handled without any additional rule.

Phase field models of brittle fracture can be classified into two families, although in practical implementations both families often yield similar numerical schemes [*Ambati et al.*, 2015]. The first family originated within the physics community on the basis of the work of *Aranson et al.* [2000], who proposed a continuum field model for mode I propagation in brittle amorphous solids inspired in the original phase field models for solidification. This idea was the seed for further developments. For instance, *Karma et al.* [2001] proposed an approach for simulating the dynamic fracture propagation in mode III, and *Henry and Levine* [2013] developed a phase field formulation for modeling fracture growth under modes I and III.

The second family emerged in the computational mechanics community, inspired in the work of *Ambrosio and Tortorelli* [1990] which proposed a phase field approximation of the Mumford-Shah potential [*Mumford and Shah*, 1989] based on Γ convergence. Motivated on these works, *Francfort and Marigo* [1998] developed a variational formulation for quasi-static fracture evolution in a brittle material based on the minimization of

the combined elastic energy in the bulk material and the fracture energy. Later, *Bourdin et al.* [2000] proposed a numerical implementation of the variational formulation. They defined the phase field as a variable which distributes the fracture energy over the bulk material. Many other authors have contributed to advancing this approach.

An alternative quasi-static formulation for brittle fracture based on continuum mechanics and thermodynamical principles was developed by *Miehe et al.* [2010a]. The formulation was later extended by the introduction of the so-called *local history field*, which ensures that the damaged region does not become unbroken even when stress disappears (that is the irreversibility of the fracture process) combined with an *operator split scheme* that successively updates the different fields involved in the formulation and permits simplifying the numerical implementation of the problem while providing a robust algorithm [*Miehe et al.*, 2010b]. The framework was also extended to study dynamic problems [*Hofacker and Miehe*, 2012, 2013]. It also has been coupled to thermomechanical problems at large strains [*Miehe et al.*, 2015a] or adapted to simulate ductile fracture coupled with thermoplasticity at finite strains [*Miehe et al.*, 2015b].

Phase field models have also been extended to model fluid-hydraulic brittle fracturing. An early contribution was made by *Bourdin et al.* [2012], who proposed a model for simulating the propagation of a fracture in a linear elastic impermeable solid. Fracture propagation was limited to the toughness-dominated regime. This model was employed to study the effect of in situ stresses over the fracture propagation path [*Chukwudozie et al.*, 2013]. Later, *Mikelic et al.* [2015a, 2015b] extended the approach to poroelastic media at small strains. In that work, both the flow equation in the medium and the fracture had the same dimensions and were governed by Darcy's law, and a permeability tensor was imposed in the fracture in order to account for the higher permeability along the crack. *Miehe et al.* [2015c] and *Miehe and Mauthe* [2016] proposed a new approach for fracture propagation in a poroelastic medium at finite strains. The phase field evolution was driven by the effective stress in the solid skeleton. Moreover, the flow in the fractures was governed by Poiseuille flow modeled through a transition rule for Darcy flow combined with an anisotropic permeability tensor.

Although the previous methods lead to straightforward computational frameworks, the storage of fluid within the fracture is approximated by the storage within the solid. The smearing effect introduced by the phase field leads to an artificial larger strain in the transition region and corresponds an artificial large storage fluid volume. Whereas this approximation may be acceptable in poroelastic solids in which the leak-off rate from the fracture to the solid may be of the same order of magnitude as the injection rate, it can result in large errors when applied to impermeable elastic solids.

Here we propose a new quasi-static formulation for modeling fluid-driven fracturing in elastic media at small strains, which describes fluid flow in the fracture and its coupling with the elastic deformation of the surrounding medium. We simulate the flow in the fracture through the Reynolds lubrication equation. The fluid pressure in the fracture, the aperture, and the deformation of the medium are solved in a fully coupled fashion employing two separate meshes which are coincident in space. This strategy allows for a careful description of the storage within the fracture. To assess the performance of phase field models for hydraulic fracturing simulation, we compare the results of the evolution of the fracture length, aperture, and fluid pressure against analytical solutions for several well-understood fracture propagation regimes.

The paper is organized as follows. Section 2 provides the governing equations for the fluid flow in the fracture and the rock mechanics with damage. A few notes on the numerical implementation of the model are given at the end of the section. A detailed description of the analytical benchmark models is included in section 3 and Appendix A. The case study where the numerical and analytical approaches are applied is described in section 4, together the results and analysis of the simulations. Finally, some conclusions are provided in section 5.

2. Governing Equations

In this section, we begin by describing the geometrical representation of the fracture/matrix domains, together with the fracture flow model, mechanical equilibrium equations and stress-strain relations. We then derive our damage propagation framework from variational principles and exploit this approach to introduce the phase field methodology for the simulation of quasi-static, brittle, fluid-driven fracture propagation in elastic materials. Finally, we summarize the analytical solutions to the problem that will be used to evaluate the numerical model results.
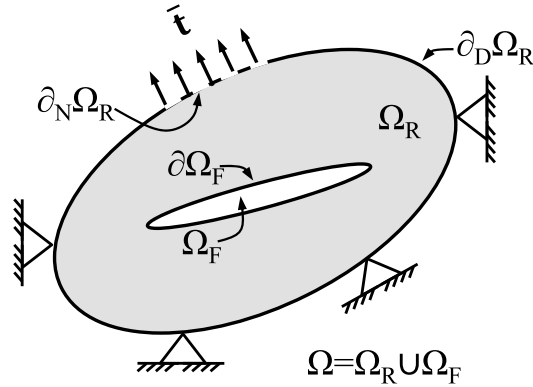
Figure 1. Schematic of the fluid-pressurized fracture domain, Ω_F, and the elastic medium domain, Ω_R.

2.1. Geometry

Consider a domain $\Omega \subset \mathfrak{R}^\delta$ with spatial dimension $\delta \in \{2, 3\}$, as depicted in Figure 1. The medium comprises an impermeable elastic subdomain, Ω_R, and a pressurized fracture subdomain, Ω_F; i.e., $\Omega = \Omega_R \cup \Omega_F$. A slightly compressible Newtonian fluid is injected inside the fracture at constant rate Q. While no mass exchange occurs between subdomains, the fluid pressure exerts a force over the elastic subdomain that can propagate the fracture. The boundary of Ω_i is denoted by $\partial\Omega_i$, where $i = R, F$. The boundary of Ω_R is divided into two subsets, $\partial_D\Omega_R$ and $\partial_N\Omega_R$, where Dirichlet and Neumann boundary conditions are imposed, respectively.

2.2. Fluid Flow in the Fracture

The fracture subdomain Ω_F is represented as a lower dimensional manifold, and fluid flow within the fracture is described through lubrication theory. The fluid motion is therefore governed by the Reynolds equation:

$$\frac{\partial w}{\partial t} + C_f w \frac{\partial p_f}{\partial t} = \nabla_s \cdot \left(K(w) \left(\nabla_s p_f - \rho_f g \nabla_s z \right) \right) + q, \tag{1}$$

where w is the fracture aperture, t is time, C_f is the compressibility of the fluid, s is the longitudinal coordinates along the fracture, p_f is the fluid pressure, ρ_f is the fluid density, g is the gravity acceleration, z is depth, q is the source or sink flow rate, and $K(w)$ is the fracture mobility, given by the local cubic law [*Witherspoon et al.*, 1980]:

$$K(w) = \frac{w^3}{12\mu_f}, \tag{2}$$

where μ_f is the fluid dynamic viscosity.

2.3. Variational Approach to Rock Damage

We adopt the Griffith interpretation to model quasi-static brittle fracture propagation, which states that the elastic energy release due to the propagation of the fracture is balanced by the newly created surface energy [*Griffith*, 1920; *Francfort and Marigo*, 1998]. The total potential energy Ψ involved in the process of fracture propagation has three contributions: the energy dissipated in the fracture process, Ψ^d; the energy stored in the bulk of the solid, Ψ^e; and the external sources of energy, Ψ^s,

$$\Psi = \Psi^d + \Psi^e - \Psi^s. \tag{3}$$

The energy dissipated in the fracture process, Ψ^d, is the work required to create a unit fracture area, i.e.,

$$\Psi^d = \int_{\partial\Omega_F} g_c \, d\partial, \tag{4}$$

where g_c is the Griffith critical energy release rate for mode I failure. This formulation requires knowing the fracture surface, which is unknown a priori. In the phase field approach, this shortcoming is remedied by the regularization of the fracture surface, i.e., by using a diffuse fracture surface defined with a phase field variable, d. This variable interpolates between the broken state ($d = 1$) and the intact one ($d = 0$). The fracture surface is then defined through and integral extended to the whole domain [*Miehe et al.*, 2010a]:

$$\Gamma_\ell = \int_\Omega \gamma_\ell \, d\Omega, \tag{5}$$

where Γ_ℓ is the regularized fracture functional and γ_ℓ is the fracture density given by

$$\gamma_\ell = \frac{1}{2\ell}d^2 + \frac{\ell}{2}\left|\nabla d\right|^2,\tag{6}$$

and ℓ is a length scale parameter. The dissipated energy, Ψ^d, reads

$$\Psi^d = \int_\Omega g_c\gamma_\ell\,\mathrm{d}\Omega,\tag{7}$$

which allows for the energy dissipated during the fracture process to be computed without prior knowledge of the discrete fracture surface.

The energy stored in the bulk of the solid, Ψ^e, evolves due to stress redistribution during deformation and due to the fracture process. The loss of stiffness of the solid due to fracture growth implies that the solid cannot store the same amount of elastic energy, and it is therefore dissipated. From a mathematical point of view, an energy transfer from Ψ^e to Ψ^d occurs. The transfer, or degradation of the elastic energy, is computed through the introduction of a degradation function, g, that depends on the phase field variable, d. While other options have been proposed, in this study we employ a quadratic degradation function [*Vignollet et al.*, 2014], since the impact of the choice of the function diminishes after the fracture has formed [*Kuhn et al.*, 2015], and the Γ convergence has so far only been proved for the quadratic polynomial [*Chambolle*, 2004]. The function has the following form:

$$g(d) = (1 - d)^2,\tag{8}$$

which assumes that the phase field variable is directly related to fracture growth.

The energy stored in the undamaged bulk of the solid Ψ_0^e is given by:

$$\Psi_0^e = \int_\Omega \psi_0^e(\varepsilon)\,\mathrm{d}\Omega,\tag{9}$$

where ψ_0^e is the undamaged elastic energy density,

$$\psi_0^e(\varepsilon) = \frac{\lambda}{2}\mathrm{tr}(\varepsilon)^2 + \mu\,\mathrm{tr}(\varepsilon^2),\tag{10}$$

where λ and μ are the Lamé constants and $\mathrm{tr}(\varepsilon)$ is the trace of the strain tensor. The degradation of the elastic energy density can be modeled mathematically in two ways. The *isotropic* damage formulation assumes degradation of the whole elastic energy as the fracture propagates [*Miehe et al.*, 2010b]:

$$\Psi^e = \int_\Omega g(d)\psi_0^e(\varepsilon)\,\mathrm{d}\Omega = \int_\Omega \psi^e(\varepsilon, d)\,\mathrm{d}\Omega.\tag{11}$$

The corresponding Cauchy stress tensor incorporating damage is therefore given by:

$$\sigma(\mathbf{u}, d) := \frac{\partial\psi^e}{\partial\varepsilon} = g(d)\frac{\partial\psi_0^e}{\partial\varepsilon}.\tag{12}$$

The above isotropic approach leads to a symmetric response of the model for fracturing under tension and compression, which may result in unrealistic fracture evolution patterns for rocks and other materials. An alternative methodology is the so-called *anisotropic* damage formulation [*Miehe et al.*, 2010b], which allows for fracturing in tension only. The formulation is suitable for hydraulic fracturing under mode I (tensile opening), and it would need to be revisited for fracture propagation under mode II (in-plane shear) or mode III (antiplane shear). The undamaged elastic energy density function, ψ_0^e, is split into a positive part, ψ_0^{e+}, due to tension, and a negative part, ψ_0^{e-}, due to compression, as follows:

$$\psi_0^e(\varepsilon) = \psi_0^{e+}(\varepsilon) + \psi_0^{e-}(\varepsilon),\tag{13}$$

where tension/compression components are defined as follows:

$$\psi_0^{e\pm}(\varepsilon) = \frac{\lambda}{2}\left(\left\langle\sum_{i=1}^{\delta}\varepsilon_i\right\rangle_\pm\right)^2 + \mu\sum_{i=1}^{\delta}\left(\langle\varepsilon_i\rangle_\pm\right)^2,\tag{14}$$

where $\pm$ refers to the tension/compression parts of the undamaged elastic energy, δ is the number of space dimensions, and $\langle x\rangle_\pm = (x \pm |x|)/2$.

This approach is based on the spectral decomposition of the strain tensor:

$$\varepsilon^{\pm}(\mathbf{u}) = \sum_{a=1}^{\delta} \langle \varepsilon_a \rangle_{\pm} \mathbf{n}_a \otimes \mathbf{n}_a, \tag{15}$$

where $\mathbf{n}_a$ is the principal strain direction associated to the principal strain ε_a. The eigenvalue bases $\mathbf{n}_a \otimes \mathbf{n}_a$ are computed in terms of the principal strains ε_i and the strain tensor ε as follows [*Miehe*, 1998]:

$$\mathbf{n}_a \otimes \mathbf{n}_a = \frac{1}{\prod_{b \neq a}^{\delta} (\varepsilon_a - \varepsilon_b)} \prod_{b \neq a}^{\delta} (\varepsilon - \varepsilon_b \mathbf{1}). \tag{16}$$

To consider degradation of the tensile energy alone, the damaged elastic energy Ψ^e is given by

$$\Psi^e = \int_{\Omega} \left[g(\mathrm{d}) \psi_0^{e+}(\varepsilon) + \psi_0^{e-}(\varepsilon) \right] \mathrm{d}\Omega = \int_{\Omega} \psi^e(\varepsilon, \mathrm{d}) \, \mathrm{d}\Omega, \tag{17}$$

and the resulting stress-strain constitutive relation yields:

$$\sigma(\mathbf{u}, d) := g(d) \frac{\partial \psi_0^{e+}}{\partial \varepsilon} + \frac{\partial \psi_0^{e-}}{\partial \varepsilon}. \tag{18}$$

Alternatively,

$$\sigma^+(\mathbf{u}, d) = g(d) \sum_{a=1}^{\delta} \left[\lambda \left\langle \sum_{i=1}^{\delta} \varepsilon_i \right\rangle_+ + 2\mu \langle \varepsilon_a \rangle_+ \right] \mathbf{n}_a \otimes \mathbf{n}_a \tag{19}$$

and

$$\sigma_0^-(\mathbf{u}) = \sum_{a=1}^{\delta} \left[\lambda \left\langle \sum_{i=1}^{\delta} \varepsilon_i \right\rangle_- + 2\mu \langle \varepsilon_a \rangle_- \right] \mathbf{n}_a \otimes \mathbf{n}_a. \tag{20}$$

The external energy functional, Ψ^s, accounts for the exchanged energy between the elastic domain Ω_R and the surrounding environment. It is given by

$$\Psi^s = \int_{\Omega} \bar{\mathbf{f}} \cdot \mathbf{u} \, \mathrm{d}\Omega + \int_{\partial_N \Omega} \bar{\mathbf{t}} \cdot \mathbf{u} \, \mathrm{d}\partial, \tag{21}$$

where $\bar{\mathbf{f}}$ is the body force per unit volume, $\bar{\mathbf{t}}$ is the vector of applied forces, and $\mathbf{u}$ is the displacement field. The second term on the right-hand side of equation (21) includes the force introduced by the pressure inside the fracture, which is applied on a surface that is a priori unknown:

$$\int_{\partial_N \Omega_F} \bar{\mathbf{t}} \cdot \mathbf{u} \, \mathrm{d}\partial = - \int_{\partial_N \Omega_F} p_f \bar{\mathbf{n}} \cdot \mathbf{u} \, \mathrm{d}\partial, \tag{22}$$

where $\bar{\mathbf{n}}$ is the normal unit vector to the fracture surface. Equation (22) can be interpreted as a flux of energy through the surface of the fracture. Using the divergence theorem, we rewrite equation (22) as

$$\int_{\partial_N \Omega_F} p_f \bar{\mathbf{n}} \cdot \mathbf{u} \, \mathrm{d}\partial = \int_{\Omega_R} \nabla \cdot (p_f \mathbf{u}) \, \mathrm{d}\Omega - \int_{\partial_N \Omega_R} p_f \bar{\mathbf{n}} \cdot \mathbf{u} \, \mathrm{d}\partial, \tag{23}$$

where the pressure exerted on the fracture is extended as a function defined over the entire domain. The practical implementation of this fictitious pressure approach is discussed in section 2.4 below. As formulated, the integral (23) is defined over the elastic medium, whose domain changes with time due to the fracture propagation. To avoid this difficulty, we introduce the degradation function, $g(d)$, and redefine the integral over the entire domain [*Mikelic et al.*, 2015b]:

$$\int_{\Omega_R} \nabla \cdot (p_f \mathbf{u}) \, \mathrm{d}\Omega = \int_{\Omega} g(d) \nabla \cdot (p_f \mathbf{u}) \, \mathrm{d}\Omega. \tag{24}$$

With the above definitions, the external energy functional finally reads:

$$\Psi^s = \int_{\Omega} \bar{\mathbf{f}} \cdot \mathbf{u} \, \mathrm{d}\Omega - \int_{\Omega} g(\mathrm{d}) \nabla \cdot (p_f \mathbf{u}) \, \mathrm{d}\Omega + \int_{\partial_N \Omega_R} p_f \bar{\mathbf{n}} \cdot \mathbf{u} \, \mathrm{d}\partial, \tag{25}$$

where we have assumed that there are no tractions applied at the domain outer boundary.

We derive the strong form of the problem via minimization of the total potential energy Ψ with respect to the displacement and phase fields, $\mathbf{u}$ and d. Herein, we have adopted the anisotropic formulation for the

degradation of the elastic energy, equation (17). The Fréchet derivative of Ψ with respect to $\mathbf{u}$ provides the elasticity, or equilibrium, equations:

$$\frac{\partial \Psi}{\partial \mathbf{u}} - \nabla \cdot \left(\frac{\partial \Psi}{\partial \nabla \mathbf{u}} \right) = \frac{\partial \Psi}{\partial \mathbf{u}} - \nabla \cdot \left(\frac{\partial \Psi}{\partial \varepsilon} \frac{\partial \varepsilon}{\partial \nabla \mathbf{u}} \right) = \mathbf{0}, \quad \text{in } \Omega, \tag{26}$$

$$\frac{\partial \Psi}{\partial \nabla \mathbf{u}} \bar{\mathbf{n}} = \bar{\mathbf{t}} + p_f \bar{\mathbf{n}}, \quad \text{in } \partial_N \Omega_R. \tag{27}$$

In terms of the positive and negative stress contributions, the equilibrium equations for the damage model are given by:

$$- \nabla \cdot \left\{ g(d) \sigma_0^+ + \sigma_0^- \right\} - p_f \nabla g(d) - \bar{\mathbf{f}} = \mathbf{0}, \quad \text{in } \Omega, \tag{28}$$

$$\sigma \bar{\mathbf{n}} = \bar{\mathbf{t}}, \quad \text{in } \partial_N \Omega. \tag{29}$$

The Fréchet derivative of Ψ with respect to d,

$$\frac{\partial \Psi}{\partial d} - \nabla \cdot \left(\frac{\partial \Psi}{\partial \nabla d} \right) = 0, \quad \text{in } \Omega, \tag{30}$$

$$\frac{\partial \Psi}{\partial \nabla d} \cdot \bar{\mathbf{n}} = 0, \quad \text{in } \partial_N \Omega \tag{31}$$

provides the Euler equations of the phase field problem:

$$\frac{g_c}{\ell} \left(d - \ell^2 \nabla^2 d \right) = 2(1-d) \left(\psi_0^{e+}(\varepsilon) + p_f \nabla \cdot \mathbf{u} + \mathbf{u} \cdot \nabla p_f \right), \quad \text{in } \Omega, \tag{32}$$

$$\nabla d \cdot \bar{\mathbf{n}} = 0, \quad \text{in } \partial_N \Omega. \tag{33}$$

The total energy density in equation (32), $\psi_0^{e+}(\varepsilon) + p_f \nabla \cdot \mathbf{u} + \mathbf{u} \cdot \nabla p_f$, determines the amount of phase field variable d at the current time. The above equation does not account for the deformation history; thus, d becomes zero when stress disappears. Introducing the maximum local history field H^+ permits accounting for the irreversibility of the process in a straightforward way [*Miehe et al.*, 2010b]. H^+ may be considered as a measure of the maximum historic tensile strain, defined as:

$$H^+(\mathbf{u}, p_f, t) = \max_{s \in [0,t]} \left(\psi_0^{e+}(\varepsilon) + p_f \nabla \cdot \mathbf{u} + \mathbf{u} \cdot \nabla p_f \right). \tag{34}$$

The Euler equation of the phase field is then written as follows:

$$\frac{g_c}{\ell} \left(d - \ell^2 \nabla^2 d \right) = 2(1-d)H^+. \tag{35}$$

2.4. Numerical Implementation of the Model

The system of governing equations comprises three partial differential equations (PDEs), modeling fluid flow inside the fracture, mechanical equilibrium, and evolution of the phase field variable. Neglecting gravity, the Reynolds lubrication equation couples the evolution of fluid pressures and fracture apertures:

$$\frac{\partial w}{\partial t} + C_f w \frac{\partial p_f}{\partial t} = \nabla_s \cdot \left(K(w) \left(\nabla_s p_f \right) \right) + q. \tag{36}$$

The second model equation is the mechanical equilibrium equation,

$$- \nabla \cdot \sigma - p_f \nabla g(d) = \mathbf{0}, \tag{37}$$

where σ is the damaged stress tensor, computed by equation (18). Finally, the third equation is the phase field equation,

$$\frac{g_c}{\ell} \left(d - \ell^2 \nabla^2 d \right) = 2(1-d)H^+, \tag{38}$$

where H^+ is given by equation (34).

Equations (36)–(38) constitute a coupled nonlinear system of equations. We adopt a finite volume scheme on a fixed regular quadrilateral mesh for the spatial discretization of the system of governing equations. As the fracture flow equation, equation (36), has a lower dimensionality in space, it is solved on a compatible regular
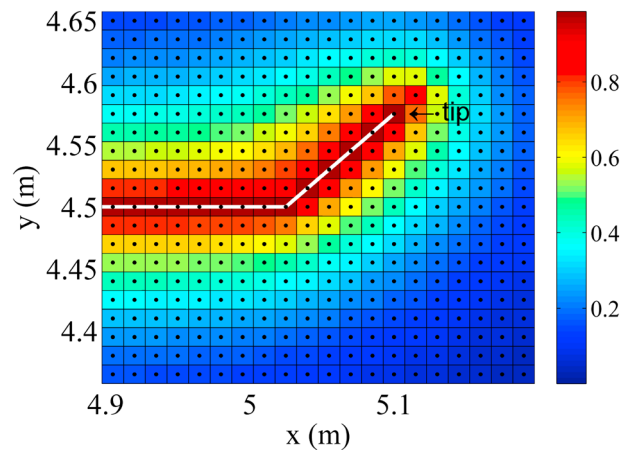
Figure 2. Propagation of the fracture. Example of contour plot of phase field variable at time t_n

one-dimensional mesh embedded in the 2-D domain. The fracture domain is defined as a lower dimensionality entity where the gradient of the phase field is zero and the phase field is above a threshold d_f: we adopt $d_f = 0.90$.

We explain the strategy through Figure 2, which draws a surface plot of d at time t_n. The mesh of the problem and the integration points are depicted in black. The fracture domain at time t_{n-1} is represented by the solid white line. To determine the fracture domain at time t_n, we first check if d is larger than d_f in the neighboring cells of the tip. If this is the case, the fracture propagates following the line that starts at the previous tip, follows the direction $\nabla d = 0$, and passes through the integration points where $d > d_f$. In Figure 2 the fracture propagates one cell, up to the point in the upper right diagonal of the tip.

We discretize equation (36) in time using a backward Euler scheme and adopt a simple two-point flux approximation in space. The aperture at point **x** along the fracture is evaluated through the line integral [*Mikelic et al.*, 2015b]

$$w(\mathbf{x}) = \int_a^b \mathbf{u}(r(\eta)) \cdot \nabla \mathrm{d}(r(\eta)) \left\| r'(\eta) \right\| \mathrm{d}\eta, \tag{39}$$

where $r(\eta)$ is the line normal to the fracture that passes through **x**. The line integral (39) has been truncated to the interval $[\mathbf{r}(a), \mathbf{r}(b)]$, whose limits denote points that are far enough from the fracture so that $\nabla d(\mathbf{r}(a))$ and $\nabla d(\mathbf{r}(b))$ are negligible.

The equilibrium equation, equation (37), includes a nonlinear stress-strain relation due to the spectral decomposition of the strain tensor, equation (15), and the presence of the phase field variable through the degradation function, equation (18). This source of nonlinearity can be handled effectively by using the so-called *hybrid* formulation for the stress-strain relationship [*Ambati et al.*, 2015], combined with a staggered scheme for updating the displacement field, **u**, and the phase field, d [*Miehe et al.*, 2010b].

The hybrid formulation for the spectral decomposition of the strain tensor contains features of the isotropic and the anisotropic formulations. The idea behind this formulation is to retain a linear equilibrium equation within a staggered scheme. The formulation requires the stress-strain relationship (12), combined with the usual phase field equation (38), where the evolution of d is driven by the tensile energy evolution Ψ_0^{e+} only. To avoid the interpenetration of rock masses on each side of the fracture, equation (38) is subjected to the constraint:

$$\forall \mathbf{x} \quad : \quad \Psi_0^{e+} < \Psi_0^{e-} \quad \Rightarrow \quad d := 0. \tag{40}$$

The above procedure switches the value of the phase field variable to zero (undamaged solid) in those areas subject to compression. When the tensile part of the energy is again larger than the compressive one, the phase field variable recovers its previous value (damaged solid) and is again driven by H^+.

Ambati et al. [2015] provide numerical evidence that the hybrid formulation leads to physical results for fracture evolution that are qualitatively and quantitatively similar to those of the anisotropic formulation, while requiring a much lower computational effort, in fact, comparable to that of the isotropic model.

Fluid pressures along the fracture contribute to the mechanical equilibrium equation, equation (37), through the body force $p_f \nabla g(d)$. Since the degradation function $g(d)$ decays quickly away from the fracture zone, this term localizes the effect of the pressure at the fracture and models the force exerted by the fluid pressure of the fracture walls. The conversion from surface to volume integrals requires, however, the ad hoc reconstruction of a pressure field extended to the full domain, not just at the fracture. In the present case of an impervious

medium, such pressure is a "fictitious" one, defined with the sole purpose of converting the impact of surface forces into body forces. In the present study, points inside the elastic domain are assigned the corresponding pressure of the closest point at the fracture. The degradation function $g(d)$ has the effect of localizing the pressure contribution, and therefore, the impact of different choices on the definition of the extended pressure is small as the fracture width decreases. We present a validation of the present approach in section 3.1.

We adopt the staggered scheme proposed by *Miehe et al.* [2010b] for computing $(\mathbf{u}, d)$, which is a simple and robust alternative to the monolithic scheme. When combined with the hybrid formulation, it provides results of comparable quality to those of the anisotropic formulation with a monolithic solution scheme [*Ambati et al.*, 2015]. However, the scheme requires sufficiently small loading increments to properly capture the nonlinearity and strong coupling of the problem. A single step of the staggered scheme in the time interval $[t_n, t_{n+1}]$ comprises three substeps:

1. Assuming that the displacements, $\mathbf{u}$, fracture pressures, p_f, phase field, d, and maximum historical energies, H^+, are known at time t_n, update H^+ with the values $\mathbf{u}_n$.
2. With the updated energy field, H^+, update the phase field variable, d.
3. Finally, advance the displacement and pressure fields $\mathbf{u}$ and p_f, using a fully coupled approach with frozen phase field d.

3. Benchmark Analytical Models

We assess the performance of our model by comparing numerical results with known analytical solutions describing asymptotic propagation regimes. To validate the fictitious pressure approach adopted here (equations (23) and (24)), we first consider the static case of a fracture subjected to a constant pressure force that is small enough to avoid growth. In the absence of fracture growth, the comparison focuses on the effect of the fracture pressure on the elastic deformations through the conversion of surface to volume forces.

We subsequently consider three fluid-driven fracture propagation cases. The analytical solutions are obtained for an infinite elastic medium under plane strain conditions: the KGD fracture (Figure 3). A far-field compression σ_0 acts in the direction perpendicular to the fracture, and an incompressible Newtonian fluid fills the fracture at constant pressure in the static case or it is injected at constant volumetric rate Q at the center of the fracture in the dynamic cases.

Further assumptions underlying the fluid-driven fracture propagation models include the following:

1. The fracture is fully filled with fluid at all times.
2. The fracture is in mobile equilibrium, and its quasi-static propagation is described in the framework of linear elastic fracture mechanics.
3. The flow of the fluid is unidirectional and laminar, and it is governed by the Reynolds lubrication equation.

Sections 3.1 and 3.2 summarize the analytical results applicable to the different tests and propagation regimes. These analytical solutions are compared with numerical ones in section 4.

3.1. Static Case

The first benchmark is the analytical solution of *Sneddon* [1946], who considered an infinite 2-D elastic domain with a fracture of constant length $2l$ filled with a fluid at pressure p_f. The fracture aperture profile, $w(x)$, is given by:

$$w(x) = \frac{4pl}{E'} \sqrt{1 - \left(\frac{x}{l}\right)^2},$$

(41)

where $p = p_f - \sigma_0$ is the net pressure, $E' = E/(1 - v^2)$, and x is the position along the fracture. This fairly simple model allows us to validate equation (23), where pressure forces are accounted for as body forces using the phase field. Moreover, we test the convergence and mesh independence of our model results by conducting a mesh refinement study. In particular, we study the effect of mesh size on the fracture aperture. We measure the discrepancy between the analytical and numerical apertures through the L_2 error norm, given by:

$$L_2 = \|V^{\text{ex}} - V^{\text{num}}\|_2 = \left\{ \sum_{i=1}^{N_i} \int_{\Omega} \left(V_i^{\text{ex}} - V_i^{\text{num}}\right)^2 \mathrm{d}s \right\}^{1/2},$$

(42)

where V_i^{ex} is the exact value of the variable at location i and V_i^{num} is the numerical value.
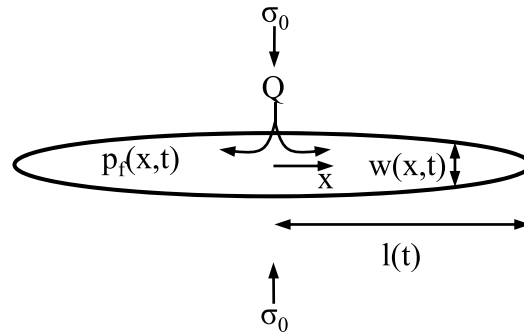
Figure 3. Schematic of a two-dimensional, fluid-driven fracture in an infinite elastic medium under plane strain conditions. The fracture is described as a lower dimensional manifold, and fluid flow through the fracture is modeled through the lubrication approximation, equation (1).

3.2. Regimes of Fracture Propagation

The propagation of a fluid-filled fracture in an elastic permeable medium is governed by two competing dissipative processes related to fluid viscosity and medium toughness and two competing storage mechanisms related to storage in the fracture and in the medium [*Hu and Garagash*, 2010]. In the case of impermeable media, the fracture is the only storage mechanism. We have chosen three analytical solutions, corresponding to the following scenarios:

1. Propagation of a fracture in an impermeable medium where the energy expended in fracturing the rock is much larger than the viscous dissipation. This regime is called *toughness dominated*.
2. Propagation of a fracture in an impermeable medium where the dissipation of energy in propagating the fracture is negligible compared to the viscous dissipation. This regime is known as *viscous dominated*.
3. Propagation of a fracture in a permeable medium where the storage of fluid in the porous medium is much larger than the storage in the fracture, and the dissipation of energy in propagating the fracture is also much larger than the viscous dissipation. This regime is referred to as *leak-off toughness dominated*.

The analytical solutions are included in Appendix A.

4. Numerical Results and Discussion

The geometry of the numerical model is depicted in Figure 4. The injection point is located at the center of the domain, and the fracture propagates following the minimum stress path, i.e., the horizontal direction. The dimensions of the domain are 90 m in the horizontal direction (x axis) and 60 m in the vertical direction (y axis). The mechanical properties of the solid are listed in Table 1. We assume plane strain conditions, and the injected fluid is incompressible and Newtonian.
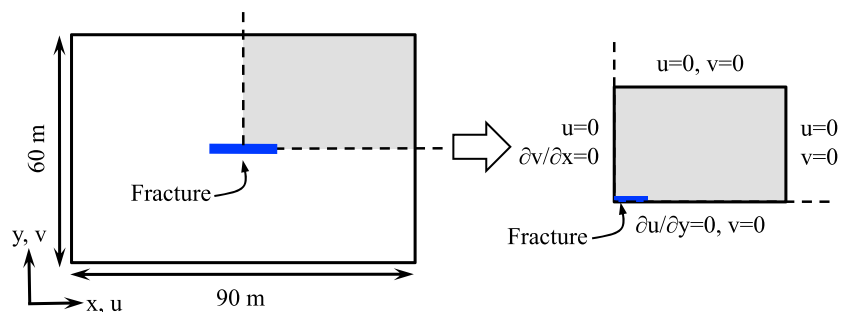

Figure 4. Model setup and boundary conditions. The injection point is located at the center of the domain, and the fracture propagates following the minimum stress path, i.e., the horizontal direction. Given that the problem is symmetric, we model one quarter of the domain only. For the x axis, the boundary conditions are zero vertical displacement, $v = 0$, and zero derivative of the horizontal displacement with respect to the vertical coordinate, $\partial u/\partial y = 0$. For the y axis, the boundary conditions are zero horizontal displacement, $u = 0$, and zero derivative of the vertical displacement with respect to the horizontal coordinate, $\partial v/\partial x = 0$. The domain is discretized using a regular square fixed mesh composed of 1.5 million cells of size $\delta x = \delta y = 0.03$ m.

Table 1. Mechanical Properties of the Elastic Medium

Young's modulus E	17 GPa
Poisson's ratio v	0.2
Griffith energy g_c	120 Pa m

The symmetry of the problem allows us to model one quarter of the domain only (Figure 4). Hence, the mechanical boundary conditions are zero displacements except in the axes of symmetry. For the x axis, the boundary conditions are zero vertical displacement, $v = 0$, and zero derivative of the horizontal displacement with respect to the vertical coordinate, $\partial u/\partial y = 0$. For the y axis, the boundary conditions are zero horizontal displacement, $u = 0$, and zero derivative of the vertical displacement with respect to the horizontal coordinate, $\partial v/\partial x = 0$. The domain is discretized using a regular square fixed mesh composed of 1.5 million cells of size $\delta x = \delta y = 0.03$ m. As the analytical solutions are obtained for an infinite domain, we confirmed that the computational domain is sufficiently large, so that boundary effects do not pollute the results.

4.1. Static Case

We compute the aperture of a fracture of half-length $l = 2$ m filled with fluid at net pressure $p_f = 2.25 \times 10^5$ Pa with several mesh sizes ranging from 0.100 to 0.017 m. The fracture is introduced by setting a large-enough
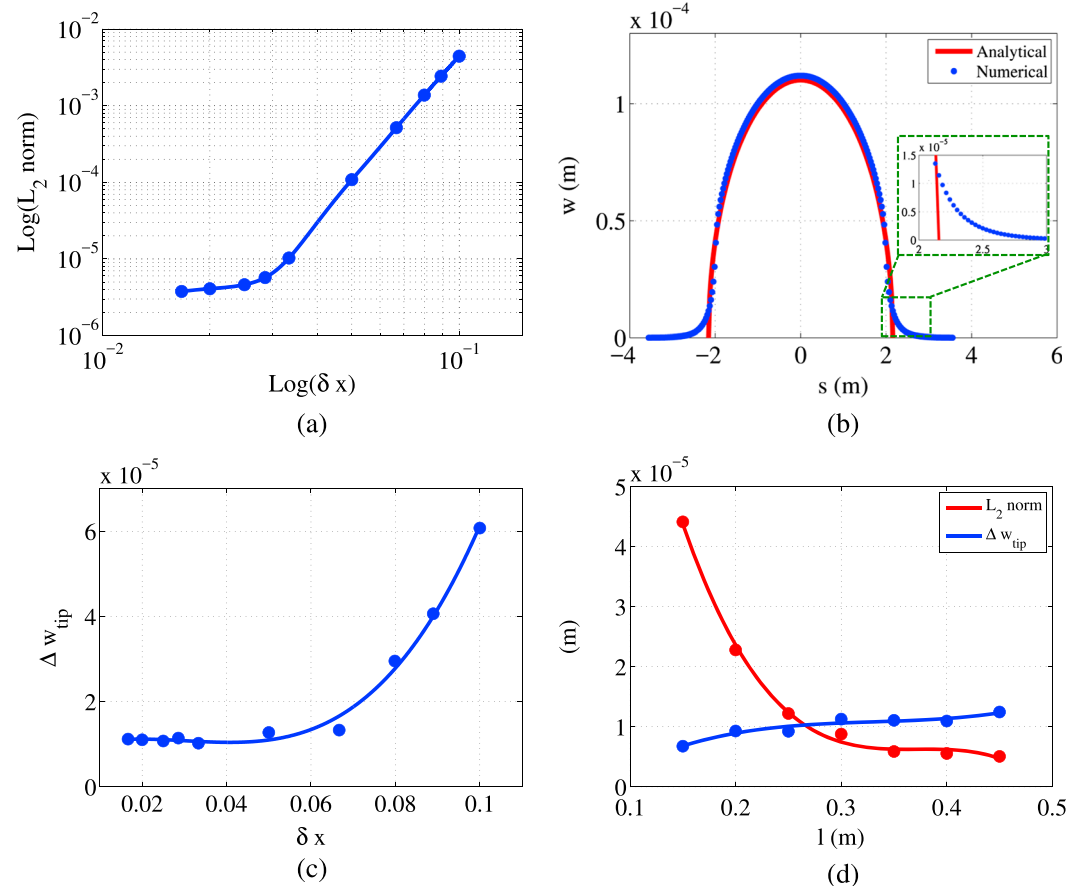

Figure 5. Static case: the Sneddon's crack. We compute the aperture of one fracture of half-length $l = 2$ m filled with fluid at pressure $p_f = 2.25 \times 10^5$ Pa and compare the results with the analytical solution of *Sneddon* [1946]. (a) We plot in log-log scale the L_2 error norm for the fracture aperture against the mesh size δ_x. (b) We plot the fracture profiles for the analytical solution and the numerical model with mesh size $\delta x = \delta y = 0.03$ m, and we zoom the fracture tip. The phase field model results agree well with the analytical solution except near the tips $(1 - \xi \rightarrow 0)$, where the phase field model introduces a smearing effect due to the regularization of the fracture surface. (c) Here we depict the deviation at the tip Δw_{tip} for several mesh sizes. We compute Δw_{tip} as the difference between the fracture aperture at the tip computed with both the analytical solution and the numerical model. (d) Setting the mesh to a size $\delta x = \delta y = 0.03$ m, as the value of ℓ increases the L_2 error norm for the fracture aperture decreases and Δw_{tip} slightly increases.

value of H^+ in the damaged region that the phase field is close to 1 in the fracture. We set the length scale parameter $\ell = 0.35$ m. We also compute the aperture profiles with the Sneddon's analytical solution [*Sneddon*, 1946].

We plot the L_2 error norm of the fracture aperture against the mesh size in log-log scale in Figure 5a. The numerical results converge to the exact solution as the element size decreases. The aperture converges quartically for the largest mesh sizes up to $\delta x = \delta y = 0.043$ m. For smaller sizes, the convergence order is lower than one. The convergence order of the aperture differs from the order of the numerical scheme—equal to 2—since the aperture is a variable computed from the solution of the numerical model. These results suggest that a good choice of the mesh size is $\delta x = \delta y = 0.03$ m. The accuracy of the numerical solution, in terms of the root-mean-square error, is 1.3×10^{-5} for this size.

To illustrate typical profiles of fracture aperture, we plot the aperture computed with the numerical model and the analytical solution (Figure 5b). The mesh size is $\delta x = \delta y = 0.03$ m. The numerical model agrees well with the analytical solution except near the fracture tips, where the phase field model does not match the exact solution due to the smearing effect introduced by the regularization of the fracture, as can be appreciated in the zoom of the tip.

To perform a quantitative assessment of the deviation near the tip owing to the diffuse modeling of the fracture, we compute the difference between the exact and the numerical aperture at the tip for several mesh sizes (Figure 5c). The deviation has the same order of magnitude as the L_2 norm, and it converges to the exact solution as the size decreases.

The distance occupied by the deviation—distance between the position of the exact tip and the point where the numerical aperture is zero—is controlled by the length scale parameter ℓ. The deviation is proportional to the transition between the broken and undamaged regions, which increases with the value of ℓ. For a given mesh size, the accuracy of the numerical model also depends on ℓ. The evolution of the L_2 error for the fracture aperture with the value of ℓ is depicted in Figure 5d. Larger values of ℓ provides more accurate apertures, but the deviation slightly increases due to the smearing effect. In the following numerical models we set $\ell = 0.35$ m.

4.2. Fracture Propagation Cases
4.2.1. Toughness-Dominated Regime
To perform a simulation in the toughness-dominated regime, we inject fluid with dynamic viscosity $\mu'_f = 10^{-6}$ Pa s at a rate $Q = 10^{-3}$ m²/s. The dimensionless viscosity $\mathcal{M}$ is equal to 1.4×10^{-4}, which is significantly less than $\mathcal{M}_0 = 3.4 \times 10^{-3}$, indicating that the fracture propagates in the desired regime. We start the simulation with an initial fracture of length 2.2 m. We do not provide initial fracture aperture or fluid pressure consistent with the analytical solutions since the net pressure depends on the far-field stress induced by the boundaries, which are initially unknown. Some discrepancies at early times arise that after some time steps disappear.

To illustrate typical model results, we plot the phase field, vertical displacements, and principal tensile stresses at time $t = 10$ s, at which the fracture has grown to a length of approximately 10 m (Figure 6). Since phase field models regularize damage and define the fracture as a diffuse interface, a small transition exists between the fractured ($d = 1$) and intact ($d = 0$) regions. This transition, whose width is controlled by the length scale parameter ℓ, is fully resolved by the computational grid (Figure 6a).

The vertical displacement field is shown in Figure 6b. The displacement is largest at the center of the fracture, and it decreases toward the fracture tips. However, the computed displacements in the transition region are artificially large as a result of the mathematical regularization of the fracture. Therefore, fracture apertures are not directly provided by the displacement fields but, rather, require the evaluation of the integral equation (39); that is, in the present diffuse interface model, fracture apertures are recovered from the displacements as a nonlocal quantity. If we were to estimate apertures directly from the displacements (Figure 6b), the aperture of the central point of the fracture is approximately 0.8 mm. In contrast, the aperture computed using equation (39) is smaller, approximately 0.6 mm.

Stress concentration occurs at both fracture tips, while inside the crack the stress is close to zero (Figure 6c). This pattern is consistent with predictions from the classical theory of linear elastic fracture mechanics. Stress is calculated through a stress-strain constitutive relation that involves the phase field variable. In turn,
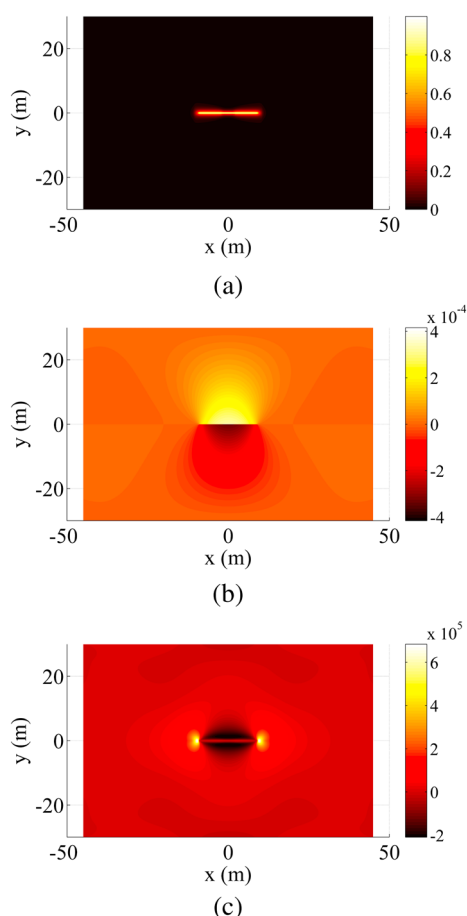
Figure 6. Toughness-dominated regime: Contour plots of (a) phase field, (b) vertical displacement, and (c) principal tensile stress, at time $t = 10$ s.

the evolution of the phase field is governed by the stress-strain constitutive relation over the undamaged solid, which provides larger stresses than the ones shown in Figure 6c.

To perform a quantitative assessment of the computational model, we plot the evolution in time of the fracture half-length $l(t)$, fracture midpoint aperture $w(x = 0, t)$, and net fluid pressure at the fracture midpoint, $p(x = 0, t)$ (Figures 7a–7c). The results from the numerical model agree well with the analytical solution presented in section A1. We limite the simulation to the point where the half-length was approximately 14 m or about 30% of the half domain, to avoid boundary effects. The agreement between simulated fracture apertures and analytical solution is excellent except at very early times, when the aperture computed by the numerical model is smaller than the analytical one (Figure 7b). This effect is due to the time needed by the numerical model to increase the fracture apertures to the point where fracture propagation starts. In that sense, the deviation from the analytical results can be attributed to an onset time. We provide more details on this issue in the next section, where we discuss the viscous-dominated case. The far-field stress σ_0 is constant in time and space in the analytical model. However, it is not in the numerical approach due to the boundary condition of zero normal displacements. We compute the net pressure as the difference between the fluid pressure and the average vertical stresses along the horizontal boundaries. The resulting pressure is slightly higher than the analytical solution, but both evolutions exhibit the same power law scaling except at the beginning of the simulation (Figure 7c).

An important characteristic of the toughness-dominated regime is the pressure distribution along the fracture. For a given time, the pressure is almost uniform in the fracture except at the fracture tip, where a significant pressure drop occurs (Figure 8a). The first-order analytical solution provides a uniform value of the
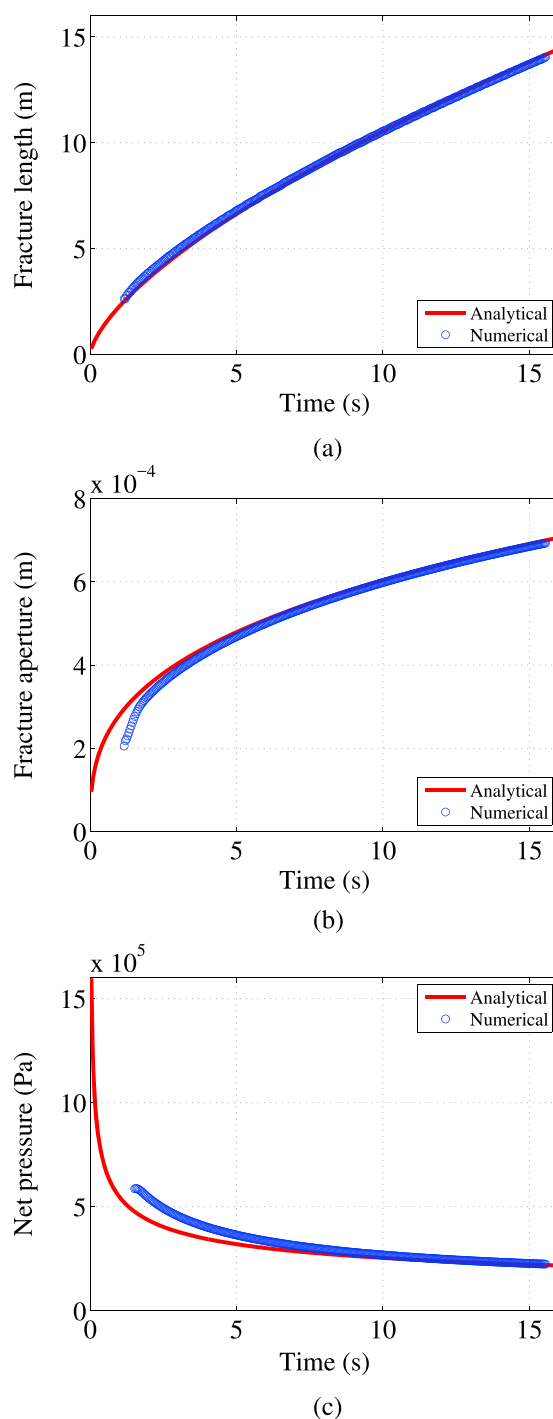
Figure 7. Toughness-dominated regime: Evolution of (a) half-length of the fracture, (b) aperture at the center of the fracture, and (c) net pressure at the center of the fracture.

pressure in the fracture (Figure 8a). The numerical model reproduces the pattern except at the fracture tip where a significant pressure drop occurs. The near-tip drop in pressure is owed to a dominance of viscous effects near the tip, where the simulated aperture is lower than the analytical one (Figure 8b) and viscous dissipation dominates.

The simulated pressure is slightly higher than the analytical solution, but the difference decreases as the fracture grows. The error is presumably owing to the far-field stress induced by the boundaries whose magnitude
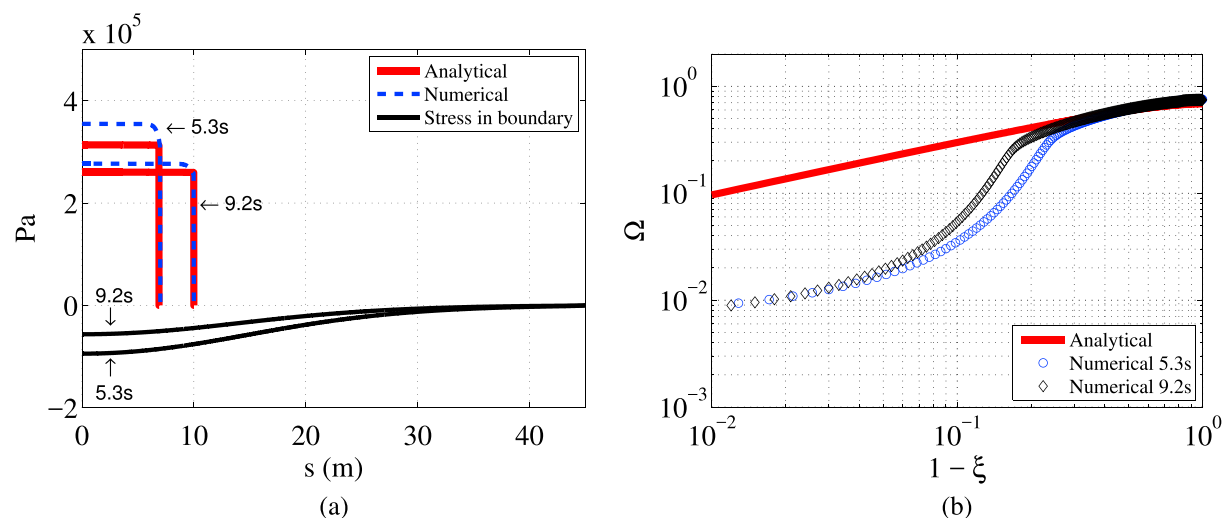
Figure 8. Toughness-dominated regime. (a) We plot the net pressure along the fracture computed with the analytical and numerical models and the vertical stress at the boundary at two different times. (b) Here we depict the dimensionless aperture against the dimensionless coordinate $\xi = x/l$ in log-log scale at the same two time steps.

becomes lower as the fracture grows and the spatial distribution is more uniform with time (Figure 8a). The numerical solution underpredicts the near-tip fracture aperture, but the error decreases as the fracture grows (Figure 8b).

4.2.2. Viscous-Dominated Regime

To perform a simulation in the viscous-dominated regime, the injection flow rate is $Q = 2 \times 10^{-4}$ m²/s and the dynamic viscosity of the fluid is $\mu'_f = 0.1$ Pa s. The initial fracture has a length of 2.2 m. Moreover, as the net pressure depends on the far-field stress induced by the boundaries, we impose an initial fracture aperture and fluid pressure lower than those from the analytical solution. After a few initial time steps, the numerical solution converges to the analytical one.

As in the previous section, we plot the evolution of the fracture half-length, aperture at the central point of the fracture, and fracture pressure at the center of the fracture (Figures 9a–9c). The numerical approach exhibits a good agreement with the analytical solution, except for minor differences at the early stages of the simulation. Initially, the pressure computed with the numerical model is lower than the one provided by the analytical formulation. Once the pressure increases and the fracture starts to grow, the pressure predicted by the numerical model agrees well with the analytical solution. Although the numerical solution slightly underpredicts the fracture pressure, both solutions show the same power law scaling after the early stages of the simulation (Figure 9c).

The reason for the discrepancy during the early stages arises from the initial value of the pressure, which is not sufficiently high in the numerical simulation. In Figure 10 we plot the fracture profiles at early times and show that during this period the fracture length does not increase. During that early period, the numerically simulated fracture "inflates" and the fluid pressure increases up to the point where the fracture starts to propagate. This onset time during which the fracture inflates prior to propagation explains, in part, the discrepancy between numerical and analytical results at early times.

The pressure distribution inside the fracture is shown in Figure 11a at two different times. In contrast with the toughness-dominated regime, the viscous-dominated regime is characterized by appreciable fluid pressure loss within the fracture which even leads to negative values of pressure. The agreement between our numerical model and the analytical solution is excellent except at the fracture tip, where the numerical solution provides lower values of the pressure because the simulated near-tip fracture aperture is smaller than the analytical one (Figure 11b). The far-field stress induced by the boundaries is smaller than in the toughness-dominated regime, which leads to better simulations of fluid pressure and fracture aperture.
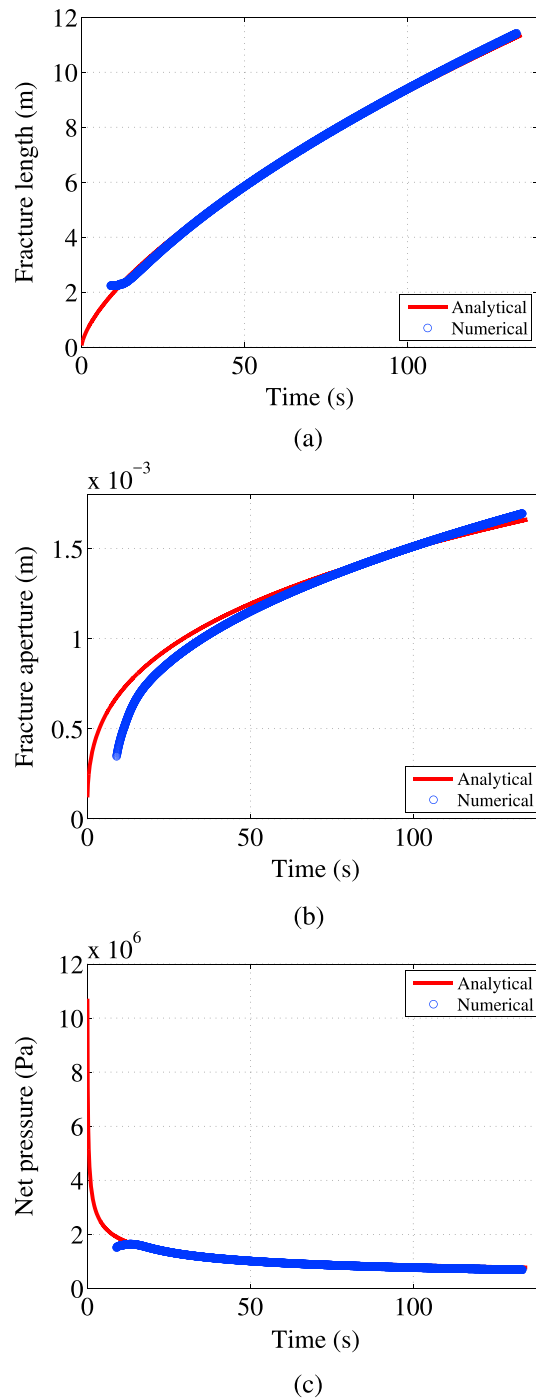
Figure 9. Viscous-dominated regime: Evolution of (a) half-length of the fracture, (b) aperture at the center of the fracture, and (c) net pressure at the center of the fracture.

4.2.3. Leak-Off Toughness-Dominated Regime

To perform a simulation in the leak-off toughness-dominated regime, we inject a fluid with dynamic viscosity $\mu'_f = 10^{-6}$ Pa s at a rate $Q = 10^{-2}$ m^2/s. The leak-off coefficient is 5×10^{-4} m/s$^{1/2}$. The initial fracture is 2.2 m length, and it is reached in the analytical solution at time 0.65 s. We impose consistent initial conditions as the Carter's model for leak-off flow rate depends on time. We calculate the initial values through an iterative process. After 0.5 s, the dimensionless time is $\tau = 1.05$, which means that the transition between the storage
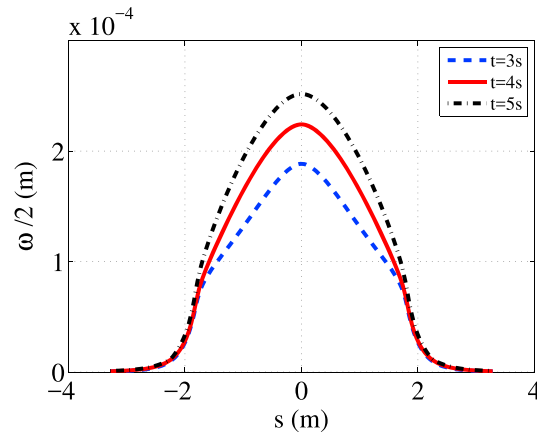
Figure 10. Viscous-dominated regime: Fracture profiles at early times. Fluid injection induces the fracture opening, but the fracture length remains constant.

and leak-off toughness-dominated regimes occurs at that moment. Since the analytical formulation indicates that the initial fracture is approximately reached at time 0.65 s, the numerical simulation starts in the leak-off regime.

The evolution of the fracture half-length, aperture at the central point of the fracture, and fracture pressure at the center of the fracture in this regime is shown in Figures 12a–12c. As was the case in the previous regimes, the phase field model prediction of the evolution of these three variables agrees well with the analytical solution. Small differences exist only during the very early stage of the simulation. It is interesting to compare the behavior of fracture propagation between this regime and the toughness-dominated regime without leak off. While the half-length at the end of the simulation is similar for both simulations, this is the result of simulations which differ by an order of magnitude in the injection flow rate: 10^{-3} m²/s for the impermeable solid and 10^{-2} m²/s. Despite the tenfold larger injection rate, the simulation with leak off results in both smaller fracture aperture and fracture fluid pressure. It is important to note that the analytical model is developed for an elastic solid in which the presence of a fluid within the pores does not alter the stress field, i.e., the Biot coefficient is zero. This feature has also been considered in the numerical model, permitting a direct comparison of the numerical results with the analytical solution.

4.3. Practical Remarks

We have simulated the propagation of fractures in homogeneous elastic solids where cracks follow planar trajectories. Phase field models enjoy the advantage that fracture nucleation, propagation, branching, or twisting
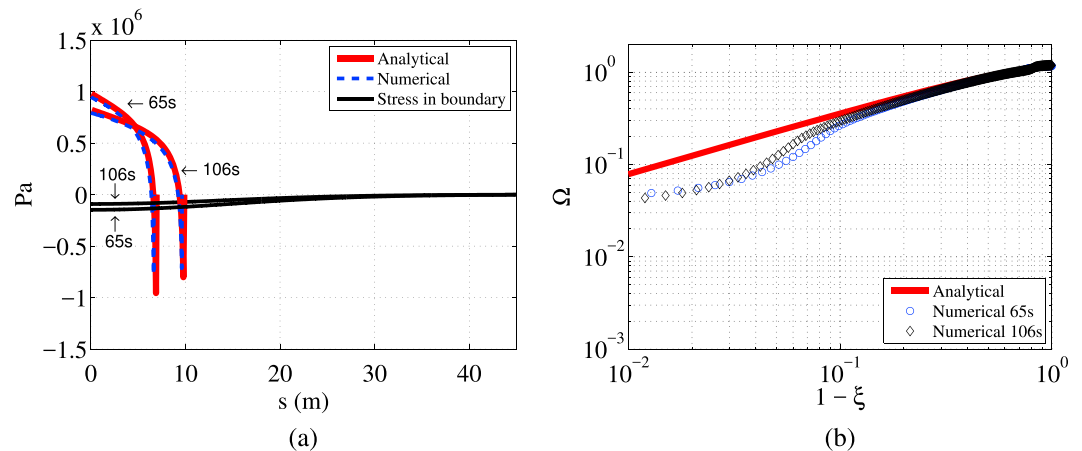

Figure 11. Viscous-dominated regime. (a) We plot the net pressure along the fracture computed with the analytical and numerical models and the vertical stress at the boundary at two different times. (b) Here we depict the dimensionless aperture against the dimensionless coordinate $\xi = x/l$ in log-log scale at the same two time steps.
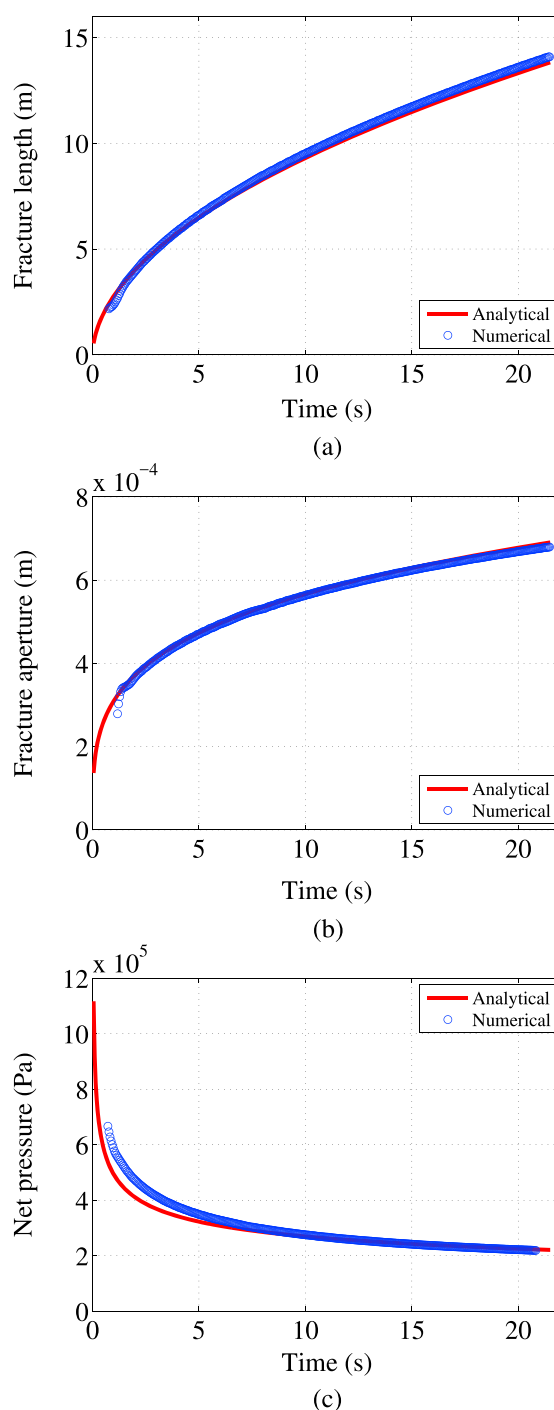
Figure 12. Leak-off toughness-dominated regime: Evolution of (a) half-length of the fracture, (b) aperture at the center of the fracture, and (c) net pressure at the center of the fracture.

can be simulated without ad hoc computational strategies. These capabilities have not been shown in the simulations of the previous section.

The method is particularly well suited to simulate fracture propagation under the toughness-dominated regime and when the injection pressure is prescribed. In this case, the pressure along the fracture is uniform and equal to the injection pressure and the injection flow rate can be computed a posteriori. This scenario is particularly suitable for determining fracture propagation patterns and constitutes a potential direction in which our method could be used.
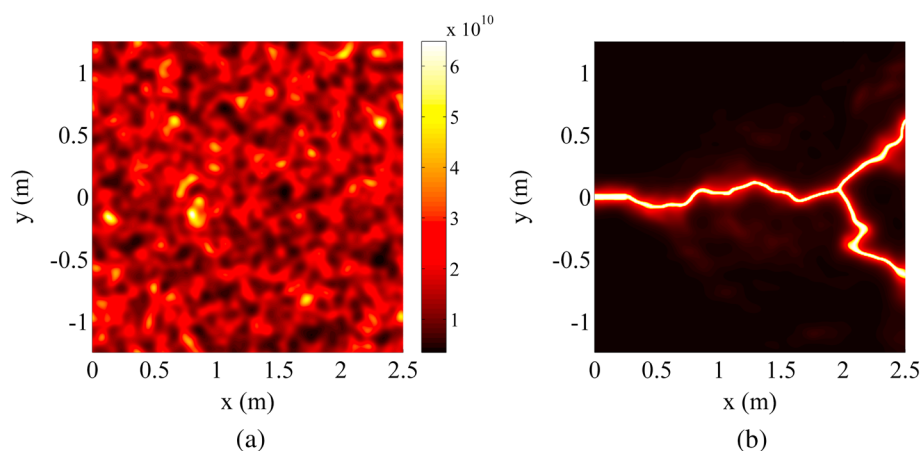
Figure 13. Toughness-dominated regime. (a) We plot one realization of 2-D lognormal Young's modulus with a Gaussian correlation function. μ_E is 17 GPa, σ_E is 6.8 GPa, and the correlation length is 0.05 m. (b) Here we depict the contour plot of the phase field. The fracture propagates in an elastic solid whose Young's modulus is depicted in the left panel.

We illustrate this with a simulation in which a fracture propagates under the toughness-dominated regime in an elastic solid where both the Young's modulus and the Griffith critical energy release rate vary spatially following isotropic lognormal fields. Both fields are assumed to have the same Gaussian correlation function $\rho(r^2)$ where r is spatial distance. We assume that at any given location $\mathbf{x}$, both the log-Griffith energy $\ln g_c(\mathbf{x})$ and the log-modulus field $\ln E(\mathbf{x})$ come from the same local value $F(\mathbf{x})$, which is an isotropic normal field with Gaussian correlation function.

We show one realization of the Young's modulus in Figure 13a. The mean value of E is 17 GPa and the standard deviation 6.8 GPa; the mean value of g_c is 120 Pa m and the standard deviation 48 Pa m. The correlation length is 0.05 m. An initial horizontal fracture of length 0.2 m is located at the center of the left side. We minimize boundary effects by embedding this domain inside a bigger square domain with sides of 60 m. We inject fluid in the initial fracture at prescribed pressure. The fracture pattern (Figure 13b) tends to follow the weakest points and results in a complex nonlinear trajectory that eventually branches into two fractures. This simulation provides an example of the capabilities of the approach to capture complex fracture patterns.

5. Conclusions

The simulation of fluid-driven fractures in geologic porous media requires a modeling framework that is able to incorporate the controlling mechanisms of fluid flow and rock fracture mechanics. Given the extreme range of spatial and temporal scales involved in these processes for realistic applications, striking a balance between physical fidelity and numerical tractability is a significant modeling challenge. Phase field method-ologies, based on the variational approach to fracture, have recently emerged as promising tools to meet that challenge, but their ability to reproduce the complex processes involved in hydraulic fracturing in realistic environments is still being debated.

The objective of the present study was to assess the performance of phase field modeling in simple injection scenarios where analytical solutions are available. Here we presented a phase field strategy to model the propagation of fluid-filled fractures in brittle elastic media and validated our approach through comparison with analytical solutions. The model considers the Reynolds lubrication equation to describe fluid flow in the fracture and linear elastic fracture mechanics. We implemented a fully coupled approach to simulate the inter-action between the pressure field in the fracture and the displacement field in the solid. We adopted a robust sequential algorithm to update damage in the solid, along with a local history field that guarantees the irre-versibility of the damage (fracture) process and an anisotropic degradation of the elastic energy which honors that fractures propagate only under tension.

We considered injection scenarios for which different propagation regimes have been identified: the toughness- and viscous-dominated regimes and the leak-off toughness regime. We compared simulated results of the evolution of fracture lengths, fluid pressures, and fracture apertures against their analytical counterparts and found good agreement in all three propagation regimes. The present validation exercise

implies that the phase field approach captures the key controlling mechanisms of coupled flow, rock mechanical deformation, and brittle fracture mechanics and therefore is a suitable tool to understand more complex processes of fluid-driven fracturing of geologic porous media.

Appendix A: Fracture Propagation. Analytical Solutions

The solution of a plane strain hydraulic fracture in an infinite elastic solid depends on the injection rate Q, the fluid dynamic viscosity μ_f, and four material parameters: Young's modulus E, Poisson's ratio ν, toughness K_{Ic}, and leak-off coefficient C_l. The formulations use the following effective material parameters:

$$E' = \frac{E}{1-\nu^2}, \quad \mu_f' = 12\mu_f, \quad K' = 4\sqrt{\frac{2}{\pi}}K_{Ic}, \quad C' = 2C_l, \tag{A1}$$

where the toughness K_{Ic} is related to the Griffith critical energy release rate g_c through

$$K_{Ic} = \sqrt{\frac{1-\nu^2}{g_c E}}. \tag{A2}$$

The pressure inside the fracture is denoted as p_f, the net pressure p is defined as $p = p_f(x,t) - \sigma_0$, the fracture opening is $w(x,t)$, and the fracture half-length is $l(t)$, where x is the position along the fracture. These variables are expressed in the following form:

$$w(x,t) = \epsilon(t)L(t)\Omega(\xi,t), \tag{A3}$$

$$p(x,t) = \epsilon(t)E'\Pi(\xi,t), \tag{A4}$$

$$l(t) = L(t)\gamma(t), \tag{A5}$$

where Ω is the dimensionless opening, Π is the dimensionless net pressure, γ is the dimensionless half-length, $\xi = x/l(t) \in [0,1]$ is the scaled coordinate, and $L(t)$ is the fracture length scale; for an impermeable solid

$$\epsilon(t) = \frac{V(t)}{L^2(t)}, \tag{A6}$$

and for a permeable one,

$$\epsilon(t) = \frac{C'^2}{Q}, \tag{A7}$$

where $\epsilon(t)$ is a characteristic fracture aspect ratio—a small dimensionless parameter which depends on the volume of injected fluid $V(t)$, among other variables.

The fluid leak off per unit fracture length is studied within Carter's model [*Carter*, 1957], which is described by an inverse square root of time law of the form

$$q(x,t) = \frac{C'}{\sqrt{t-t_0(x)}}, \quad t - t_0(x) > 0, \tag{A8}$$

where t_0 is the time at which the fracture first propagates to a given point of coordinate x.

A1. Toughness-Dominated Regime

Garagash [2006] provides an explicit solution for a fracture propagating in an impermeable elastic media in the toughness-dominated regime. The fracture length scale $L_k(t)$ is given by

$$L_k = \left(\frac{E'Q_0 t}{K'}\right)^{2/3}, \tag{A1.1}$$

where the subscript k denotes the regime. The dimensionless viscosity $\mathcal{M}$ is defined as

$$\mathcal{M} = \frac{\mu'Q}{E'}\left(\frac{E'}{K'}\right)^4. \tag{A1.2}$$

A threshold value of the viscosity for this propagation regime is $\mathcal{M}_0 = 3.4 \times 10^{-3}$, and this regime implies that $\mathcal{M} < \mathcal{M}_0$.

The solution of the problem is given by a series expansion in the small parameter $\mathcal{M}$,

$$\mathcal{F}(\mathcal{M}, \xi) = \sum_{j=0}^{\infty} \mathcal{M}^j \mathcal{F}_j(\xi) \tag{A1.3}$$

with $\mathcal{F}_j(\xi) = \{\bar{\Omega}_{kj}(\xi), \Pi_{kj}(\xi), \gamma_{kj}\}$, and $\bar{\Omega}_{kj}(\xi) = \Omega_{kj}(\xi)/\gamma_k(t)$, combined with equations (A3)–(A5). The zeroth-order solution, i.e., the first term in the expansion or $j = 0$, is the zero-viscosity solution. The first-order solution, $j = 0, 1$, provides the correction of order $\mathcal{M}$ to the zero-viscosity solution and is denoted as the *small viscosity solution* or *large toughness solution*. *Garagash* [2006] points out that the first-order solution provides an excellent approximation for a wide range of the viscosity parameter. Moreover, he improved this solution and proposed a new formulation in terms of the small parameter $\delta(\mathcal{M})$

$$\delta(\mathcal{M}) = \frac{\mathcal{M}}{\sqrt{1 + \mathcal{M}/\mathcal{M}_{Si}}}, \tag{A1.4}$$

where $\mathcal{M}_{Si} = 1/30$. The improved first-order solution has the form

$$\mathcal{F}(\mathcal{M}, \xi) = \mathcal{F}_0(\xi) + \delta(\mathcal{M})\mathcal{F}_1(\xi). \tag{A1.5}$$

The zeroth-order dimensionless variables are given by

$$\bar{\Omega}_{k0}(\xi) = \frac{\pi^{1/3}}{2}\sqrt{1 - \xi^2}, \tag{A1.6}$$

$$\Pi_{k0} = \frac{\pi^{1/3}}{8}, \tag{A1.7}$$

$$\gamma_{k0} = \frac{2}{\pi^{2/3}} \tag{A1.8}$$

and the first-order variables by

$$\bar{\Omega}_{k1}(\xi) = \frac{8}{3\pi^{2/3}} \left(2\pi - 4\xi \arcsin\xi - \left(\frac{5}{6} - \ln 2\right)\sqrt{1 - \xi^2} - \frac{3}{2}\ln\left|\frac{\left(1 + \sqrt{1 - \xi^2}\right)^{1+\sqrt{1-\xi^2}}}{\left(1 - \sqrt{1 - \xi^2}\right)^{1-\sqrt{1-\xi^2}}}\right| \right), \tag{A1.9}$$

$$\Pi_{k1} = \frac{8}{3\pi^{2/3}} \left(\frac{1}{24} + \ln\left(4\sqrt{1 - \xi^2}\right) - \frac{3\xi \arccos\xi}{4\sqrt{1 - \xi^2}} \right), \tag{A1.10}$$

$$\gamma_{k1} = -\frac{32(1 + 6\ln 2)}{9\pi^{5/3}}. \tag{A1.11}$$

A2. Viscous-Dominated Regime

An explicit analytical solution for the problem of fluid-driven fracturing in an impermeable elastic media in the viscous-dominated regime was found by *Adachi and Detournay* [2002] and *Garagash and Detournay* [2005]. The fracture length scale $L_m(t)$ is given by

$$L_m = \left(\frac{E'Q^3t^4}{\mu'}\right)^{1/6}, \tag{A2.1}$$

where the subscript m denotes the regime. The dimensionless toughness $\mathcal{K}$ is given by

$$\mathcal{K} = \frac{K'}{E'}\left(\frac{E'}{\mu'Q}\right)^{1/4}. \tag{A2.2}$$

A threshold value of the toughness for this propagation regime is $\mathcal{K}_0 = 1.42$, with a range of validity $\mathcal{K} < \mathcal{K}_0$.

As in the toughness-dominated regime, the solution of the problem is given by a series expansion in the parameter $\mathcal{E}(\mathcal{K})$,

$$\mathcal{F}(\mathcal{K}, \xi) = \sum_{j=0}^{\infty} \mathcal{E}(\mathcal{K})^j \mathcal{F}_j(\xi), \tag{A2.3}$$

with $\mathcal{F}_j(\xi) = \{\bar{\Omega}_{mj}(\xi), \Pi_{mj}(\xi), \gamma_{mj}\}$, and $\bar{\Omega}_{mj}(\xi) = \Omega_{mj}(\xi)/\gamma_m(t)$, combined with equations (A3)–(A5). The parameter $\mathcal{E}(\mathcal{K})$ will be defined later. The zeroth-order solution, $j = 0$, is the zero-toughness solution.

The first-order solution, $j = 0, 1$, provides the correction of order $\mathcal{E}(\mathcal{K})$ to the zero-toughness solution and is denoted as the *small toughness solution* or *large viscosity solution*. As shown in *Garagash and Detournay* [2005], the first-order solution provides an excellent approximation.

The zeroth-order dimensionless variables are given by *Adachi and Detournay* [2002]:

$$\bar{\Omega}_{m0}(\xi) = A_{00}(1 - \xi^2)^{2/3} + A_{01}(1 - \xi^2)^{5/3} + B_{01}\left[4\sqrt{1 - \xi^2} + 2\xi^2 \ln\left|\frac{1 - \sqrt{1 - \xi^2}}{1 + \sqrt{1 - \xi^2}}\right|\right],$$
(A2.4)

$$\Pi_{m0}(\xi) = A_{00}\frac{1}{3\pi}B\left(\frac{1}{2}, \frac{2}{3}\right){}_2F_1\left(-\frac{1}{6}, 1; \frac{1}{2}, \xi^2\right) + A_{01}\frac{10}{7}{}_2F_1\left(-\frac{7}{6}, 1; \frac{1}{2}, \xi^2\right) + B_{01}(2 - \pi\,|\xi|),$$
(A2.5)

$$\gamma_{m0} = 0.61524,$$
(A2.6)

where $A_{00} = \sqrt{3}$, $A_{01} \approx -0.15601$, $B_{01} \approx 6.632 \times 10^{-2}$, $B(\cdot, \cdot)$ is the Euler's beta function, and ${}_2F_1(\cdot, \cdot; \cdot, \cdot)$ is the Gauss hypergeometric function.

The first-order dimensionless variables read as follows [*Garagash and Detournay*, 2005]:

$$\bar{\Omega}_{m1}(\xi) = A_{10}(1 - \xi^2)^h + A_{11}(1 - \xi^2)^{h+1}C_2^{h+1/2}(\xi) + B_{11}\left[4\sqrt{1 - \xi^2} + 2\xi^2 \ln\left|\frac{1 - \sqrt{1 - \xi^2}}{1 + \sqrt{1 - \xi^2}}\right|\right],$$
(A2.7)

$$\begin{aligned}
\Pi_{m1}(\xi) = &A_{10}\frac{\Gamma(1 + h)}{2\pi^{1/2}\Gamma\left(\frac{1}{2} + h\right)}{}_2F_1\left(\frac{1}{2} - h, 1; \frac{1}{2}, \xi^2\right) \\
&+ A_{11}\frac{-1}{B\left(\frac{1}{2} + h, \frac{3}{2}\right)}\left[\frac{1}{2}{}_2F_1\left(-\frac{3}{2} - h, 1; \frac{1}{2}, \xi^2\right) - (1 + h)\xi^2{}_2F_1\left(-\frac{1}{2} - h, 2; \frac{3}{2}, \xi^2\right)\right] \\
&+ B_{11}(2 - \pi\,|\xi|),
\end{aligned}$$
(A2.8)

$$\gamma_{m1} = -\frac{1}{2}\gamma_{m0}^3\left[A_{10}B\left(\frac{1}{2}, 1 + h\right) - A_{11}\frac{1/2 + h}{5/2 + h}B\left(\frac{1}{2}, 2 + h\right) + B_{11}\frac{4\pi}{3}\right],$$
(A2.9)

where $h \approx 0.138673$, $C_2^{(\kappa)}(\cdot)$ is the Gegenbauer polynomial of degree 2 and index κ, $A_{10} = 2^{-h}$, $A_{11} \approx -4.0042 \times 10^{-2}$, $B_{11} \approx -4.5476 \times 10^{-2}$, and $\Gamma(\cdot)$ is the Euler gamma function.

The Gegenbauer polynomial of degree n and index κ, $C_n^{(\kappa)}(\cdot)$, has the form

$$C_n^{(\kappa)}(x) = \sum_{k=0}^{n/2}(-1)^k\frac{\Gamma(n - k + \kappa)}{\Gamma(\kappa)k!(n - 2k)!}(2x)^{n-2k}.$$
(A2.10)

Finally, the parameter $\mathcal{E}(\mathcal{K})$ is defined as

$$\mathcal{E}(\mathcal{K}) = B_1\mathcal{K}^b,$$
(A2.11)

where b and $\bar{B}_1$ are computed from the constants γ_{m0}, h, and $\beta_1 \approx 0.03719$ according to

$$b = 4 - 6h \approx 3.16796$$
(A2.12)

and

$$B_1 = \left(\frac{2}{3}\right)^{2h-1}\gamma_0^{3h-2}\beta_1 \approx 0.1076.$$
(A2.13)

A3. Leak-Off Toughness-Dominated Regime

Bunger et al. [2005] consider the problem of the propagation of a fracture by a zero fluid viscosity in a permeable medium. The authors studied the so-called *small and large time asymptotic behaviors*, which correspond to the storage toughness-dominated regime and leak-off toughness-dominated regime, respectively. During fracture growth, the propagation evolves in time and transitions from the storage toughness-dominated regime to the leak-off toughness-dominated regime.

The fracture length scale $L_{k,\tilde{k}}(t)$ is given by

$$L_{k,\tilde{k}} = \left(\frac{K'Q}{E'C'^2} \right)^2, \tag{A3.1}$$

where the subscript k or $\tilde{k}$ denotes the regime. The dimensionless viscosity $\mathcal{M}_{k,\tilde{k}}$ is defined as

$$\mathcal{M}_{k,\tilde{k}} = \frac{\mu'QE'^3}{K'^4}, \tag{A3.2}$$

and the dimensionless time τ is defined as

$$\tau = t\frac{E'^4 C'^2}{K'^4 Q^2}. \tag{A3.3}$$

The solution obtained by the authors is valid when $\mathcal{M}_{k,\tilde{k}} \ll 1$.

For $\tau \ll 1$, the fracture propagates under the storage toughness-dominated regime. The dimensionless variable γ_k is then given by

$$\gamma_k(\tau) = \tau^{2/3} \sum_{i=0}^{n} \gamma_{ki}\tau^{-i/6}, \tag{A3.4}$$

where

$$\gamma_{k0} = \frac{2}{\pi^{2/3}}, \tag{A3.5}$$

$$\gamma_{k1} = -\frac{16 I_{2/3}}{3\pi^{4/3}}, \tag{A3.6}$$

$$\gamma_{k2} = \frac{32 I_{2/3}}{9\pi^2}\left(I_{2/3} - 4I_{5/6} \right), \tag{A3.7}$$

$$\gamma_{k3} = -\frac{512 I_{2/3}}{81\pi^{8/3}}\left[-8I_{5/6} + I_{2/3}\left(2 - I_{2/3} + 3I_{5/6} \right) \right], \tag{A3.8}$$

and I_φ is an integral solved in terms of the Gamma function $\Gamma(\cdot)$ as

$$I_\varphi = \int_0^1 \frac{\eta^\varphi}{\sqrt{1-\eta}}\,\mathrm{d}\eta = \frac{\Gamma(\varphi+1)\Gamma(1/2)}{\Gamma(\varphi+3/2)}. \tag{A3.9}$$

For $\tau \gg 1$, the propagating regime has evolved to the leak-off toughness-dominated regime. The dimensionless variable $\gamma_{\tilde{k}}$ is now given by

$$\gamma_{\tilde{k}}(\tau) = \sqrt{\tau} \sum_{i=0}^{n} \gamma_{\tilde{k}i}\tau^{-i/4}, \tag{A3.10}$$

where

$$\gamma_{\tilde{k}0} = \frac{1}{\pi}, \tag{A3.11}$$

$$\gamma_{\tilde{k}1} = -\frac{1}{4\sqrt{2\pi}I_{1/4}}, \tag{A3.12}$$

$$\gamma_{\tilde{k}2} = \frac{3}{128 I_{1/4}}, \tag{A3.13}$$

$$\gamma_{\tilde{k}3} = -\frac{3\sqrt{\pi}(1 + 3I_{1/4})}{1024\sqrt{2}I_{-1/4}I_{1/4}^2}. \tag{A3.14}$$

The dimensionless opening and pressure are given as

$$\Omega_{k,\tilde{k}} = 2^{-1/2}\gamma^{(1/2)}\sqrt{1 - \xi^2} \tag{A3.15}$$

and

$$\Pi_{k,\tilde{k}} = 2^{-5/2}\gamma^{-1/2}. \tag{A3.16}$$

References

Adachi, J. I., and E. Detournay (2002), Self-similar solution of a plane-strain fracture driven by a power-law fluid, *Int. J. Numer. Anal. Methods Geomech.*, *26*(6), 579–604.

Adachi, J. I., and E. Detournay (2008), Plane strain propagation of a hydraulic fracture in a permeable rock, *Eng. Fract. Mech.*, *75*(16), 4666–4694.

Ambati, M., T. Gerasimov, and L. De Lorenzis (2015), A review on phase-field models of brittle fracture and a new fast hybrid formulation, *Comput. Mech.*, *55*, 383–405.

Ambrosio, L., and V. M. Tortorelli (1990), Approximation of functional depending on jumps by elliptic functional via Γ-convergence, *Commun. Pure Appl. Math.*, *43*, 999–1036.

Aranson, I. S., V. A. Kalatsky, and V. M. Vinokur (2000), Continuum field description of crack propagation, *Phys. Rev. Lett.*, *85*, 118–121.

Bunger, A. P., E. Detournay, and D. I. Garagash (2005), Toughness-dominated hydraulic fracture with leak-off, *Int. J. Fract.*, *134*, 175–190.

Bouchard, P. O., F. Bay, and Y. Chastel (2003), Numerical modelling of crack propagation: Automatic remeshing and comparison of different criteria, *Comput. Methods Appl. Mech. Eng.*, *192*, 3887–3908.

Bourdin, B., G. A. Francfort, and J. J. Marigo (2000), Numerical experiments in revisited brittle fracture, *J. Mech. Phys. Solids*, *48*, 797–826.

Bourdin, B., C. P. Chukwudozie, and K. Yoshioka (2012), A variational approach to the numerical simulation of hydraulic fracturing, in *SPE Annual Technical Conference and Exhibition*, Soc. of Pet. Eng., SPE-159154-MS, San Antonio, Tex.

Cappa, F., and J. Rutqvist (2011), Modeling of coupled deformation and permeability evolution during fault reactivation induced by deep underground injection of CO_2, *Int. J. Greenhouse Gas Control*, *5*(2), 336–346.

Carrier, B., and S. Granet (2012), Numerical modeling of hydraulic fracture problem in permeable medium using cohesive zone model, *Eng. Fract. Mech.*, *79*, 312–328.

Carter, E. D. (1957), Optimum fluid characteristics for fracture extension, in *Drilling and Production Practice*, edited by G. C. Howard and C. R. Fast, pp. 261–270, Am. Pet. Inst., New York.

Chambolle, A. (2004), An approximation result for special functions with bounded deformation, *J. Math. Pures Appl.*, *83*, 929–954.

Chukwudozie, C., B. Bourdin, and K. Yoshioka (2013), A variational approach to the modeling and numerical simulation of hydraulic fracturing under in-situ stresses, in *Proceedings of the 38th Workshop on Geothermal Reservoir Engineering*, Stanford Geothermal Program, Stanford, Calif.

Cueto-Felgueroso, L., and R. Juanes (2013), Forecasting long-term gas production from shale, *Proc. Natl. Acad. Sci. U.S.A.*, *110*(49), 19660–19661.

Detournay, E. (2004), Propagation regimes of fluid-driven fractures in impermeable rocks, *Int. J. Geomech.*, *4*(1), 35–45.

Detournay, E. (2016), Mechanics of hydraulic fractures, *Annu. Rev. Fluid Mech.*, *48*, 311–339.

Economides, M. J., and K. G. Nolte (2000), *Reservoir Stimulation*, 3rd ed., Wiley, Chichester, West Sussex, U. K.

Evans, K. F., H. Moriya, H. Niitsuma, R. H. Jones, W. S. Phillips, A. Genter, J. Sausse, R. Jung, and R. Baria (2005), Microseismicity and permeability enhancement of hydrogeologic structures during massive fluid injections into granite at 3 km depth at the Soultz HDR site, *Geophys. J. Int.*, *160*(1), 388–412.

Francfort, G. A., and J. J. Marigo (1998), Revisiting brittle fracture as an energy minimization problem, *J. Mech. Phys. Solids*, *46*, 1319–1342.

Fu, P., S. M. Johnson, and C. R. Carrigan (2013), An explicitly coupled hydro-geomechanical model for simulating hydraulic fracturing in arbitrary discrete fracture networks, *Int. J. Numer. Anal. Methods Geomech.*, *37*, 2278–2300.

Garagash, D. I. (2006), Plane-strain propagation of a fluid-driven fracture during injection and shut-in: Asymptotics of large toughness, *Eng. Fract. Mech.*, *73*(4), 456–481.

Garagash, D. I., and E. Detournay (2005), Plane-strain propagation of a fluid-driven fracture: Small toughness solution, *J. Appl. Mech.*, *72*(6), 916–928.

Geertsma, J., and P. De Klerk (1969), A rapid method of predicting width and extent of hydraulically induced fractures, *J. Pet. Technol.*, *246*, 1571–1581.

Griffith, A. A. (1920), The phenomena of rupture and flow in solids, *Philos. Trans. R. Soc.*, *A221*, 163–198.

Hafver, A., E. Jettestuen, J. Feder, P. Meakin, and A. Malthe-Sørenssen (2014), A node-splitting discrete element model for fluid-structure interaction, *Physica A*, *416*, 61–79.

Henry, H., and H. Levine (2013), Dynamic instabilities of fracture under biaxial strain using a phase field model, *Phys. Rev. Lett.*, *93*, 105504.

Hofacker, M., and C. Miehe (2012), Continuum phase field modeling of dynamic fracture: Variational principles and staggered FE implementation, *Int. J. Fract.*, *178*, 113–129.

Hofacker, M., and C. Miehe (2013), A phase field model of dynamic fracture: Robust field updates for the analysis of complex crack patterns, *Int. J. Numer. Methods Eng.*, *93*, 276–301.

Hu, J., and D. I. Garagash (2010), Plane-strain propagation of a fluid-driven crack in a permeable rock with fracture toughness, *J. Eng. Mech*, *136*(9), 1152–1166.

Jeffrey, R. G., and K. W. Mills (2000), Hydraulic fracturing applied to inducing longwall coal mine goaf falls, in *Pacific Rocks 2000 — Proceedings of the 4th North American Rock Mechanics Symposium*, edited by J. Girard et al., pp. 423–430, Balkema, Rotterdam, Netherlands.

Jha, B., and R. Juanes (2014), Coupled multiphase flow and poromechanics: A computational model of pore-pressure effects on fault slip and earthquake triggering, *Water Resour. Res.*, *50*, 3776–3808, doi:10.1002/2013WR015175.

Karma, A., D. A. Kessler, and H. Levine (2001), Phase-field model of mode III dynamic fracture, *Phys. Rev. Lett.*, *87*, 45501.

Khristianovich, S. A., and Y. P. Zheltov (1955), Formation of vertical fractures by means of highly viscous liquid, in *Proceeding 4th World Petroleum Congress*, vol. 2, pp. 556–579, World Petroleum Congress, Rome.

Kuhn, C., A. Schlüte, and R. Müller (2015), On degradation functions in phase field fracture models, *Comput. Mater. Sci.*, *108*, 374–384.

Kuuskraa, V., S. H. Stevens, and K. D. Moodhe (2013), *Technically Recoverable Shale Oil and Shale Gas Resources: An Assessment of 137 Shale Formations in 41 Countries Outside the United States*, U.S Energy Inform. Administr., Washington, D. C.

Legarth, B., E. Huenges, and G. Zimmermann (2005), Hydraulic fracturing in a sedimentary geothermal reservoir: Results and implications, *Int. J. Rock Mech. Min. Sci.*, *42*(7), 1028–1041.

Miehe, C. (1998), Comparison of two algorithms for the computation of fourth-order isotropic tensor functions, *Comput. Struct.*, *66*, 37–43.

Miehe, C., F. Welschinger, and M. Hofacker (2010a), Thermodynamically consistent phase-field models of fracture: Variational principles and multi-field FE implementations, *Int. J. Numer. Methods Eng.*, *83*, 1273–1311.

Miehe, C., M. Hofacker, and F. Welschinger (2010b), A phase field model for rate-independent crack propagation: Robust algorithmic implementation based on operator splits, *Comput. Methods Appl. Mech. Eng.*, *199*, 2765–2778.

Miehe, C., L. M. Schänzel, and H. Ulmer (2015a), Phase field modeling of fracture in multi-physics problems. Part I. Balance of crack surface and failure criteria for brittle crack propagation in thermo-elastic solids, *Comput. Methods Appl. Mech. Eng.*, *294*, 449–485.

Miehe, C., M. Hofacker, L. M. Schänzel, and F. Aldakheel (2015b), Phase field modeling of fracture in multi-physics problems. Part II. Coupled brittle-to-ductile failure criteria and crack propagation in thermo-elastic-plastic solids, *Comput. Methods Appl. Mech. Eng.*, *294*, 486–522.

Miehe, C., S. Mauthe, and S. Teichtmeister (2015c), Minimization principles for the coupled problem of Darcy-Biot-type fluid transport in porous media linked to phase field modeling of fracture, *J. Mech. Phys. Solids*, *82*, 186–217.

Miehe, C., and S. Mauthe (2016), Phase field modeling of fracture in multi-physics problems. Part III. Crack driving forces in hydro-poro-elasticity and hydraulic fracturing of fluid-saturated porous media, *Comput. Methods Appl. Mech. Eng.*, *304*, 619–655.

Mikelic, A., M. F. Wheeler, and T. Wick (2015a), A phase-field method for propagating fluid-filled fractures coupled to a surrounding porous medium, *Multiscale Model. Simul.*, *13*(1), 367–398.

Mikelic, A., M. F. Wheeler, and T. Wick (2015b), A quasi-static phase-field approach to pressurized fractures, *Nonlinearity*, *28*(5), 1371–1399.

Mumford, D., and J. Shah (1989), Optimal approximations by piecewise smooth functions and associated variational problems, *Commun. Pure Appl. Math.*, *42*, 577–685.

Murdoch, L. C. (2002), Mechanical analysis of idealized shallow hydraulic fracture, *J. Geotech. Geoenviron. Eng.*, *128*(6), 488–495.

Nordgren, R. P. (1972), Propagation of a vertical hydraulic fracture, *Soc. Pet. Eng. J.*, *12*, 306–314.

Oliver, J., A. E. Huespe, and P. J. Sánchez (2006), A comparative study on finite elements for capturing strong discontinuities: E-FEM vs X-FEM, *Comput. Methods Appl. Mech. Eng.*, *195*, 4732–4752.

Osborn, S. G., A. Vengosh, N. R. Warner, and R. B. Jackson (2011), Methane contamination of drinking water accompanying gas-well drilling and hydraulic fracturing, *Proc. Natl. Acad. Sci. U.S.A.*, *108*(20), 8172–8176.

Ouchi, H., A. Katiyar, J. York, J. T. Foster, and M. M. Sharma (2015), A fully coupled porous flow and geomechanics model for fluid driven cracks: A peridynamics approach, *Comput. Mech.*, *55*, 561–576.

Parmigiani, A., S. Faroughi, C. Huber, O. Bachmann, and Y. Su (2016), Bubble accumulation and its role in the evolution of magma reservoirs in the upper crust, *Nature*, *532*(7600), 492–495.

Patzek, T. W., F. Male, and M. Marder (2013), Gas production in the Barnett Shale obeys a simple scaling theory, *Proc. Natl. Acad. Sci. U.S.A.*, *110*(49), 19,731–19,736.

Perkins, T. K., and L. R. Kern (1961), Widths of hydraulic fractures, *J. Petrol. Technol.*, *13*, 937–949.

Rubin, A. M. (1995), Propagation of magma-filled cracks, *Annu. Rev. Earth Planet. Sci.*, *23*, 287–336.

Rungamornrat, J., M. F. Wheeler, and M. E. Mear (2005), A numerical technique for simulating nonplanar evolution of hydraulic fractures, in *Proceedings—SPE Annual Technical Conference and Exhibition*, pp. 3813–3821, SPE, Dallas, Tex.

Shojaei, A., A. D. Taleghani, and G. Li (2014), A continuum damage failure model for hydraulic fracturing of porous rocks, *Int. J. Plast.*, *59*, 199–212.

Sneddon, I. (1946), The distribution of stress in the neighbourhood of a crack in an elastic solid, *Proc. R. Soc. A*, *187*, 229–260.

Spence, D. A., and D. L. Turcotte (1985), Magma-driven propagation of cracks, *J. Geophys. Res.*, *90*(B1), 575–580.

Vidic, R. D., S. L. Brantley, J. M. Vandenbossche, D. Yoxtheimer, and J. D. Abad (2013), Impact of shale gas development on regional water quality, *Science*, *340*(6134), 1235009.

Vignollet, J., S. May, R. De Borst, and C. V. Verhoosel (2014), Phase-field models for brittle and cohesive fracture, *Meccanica*, *49*, 2587–2601.

Wangen, M. (2011), Finite element modeling of hydraulic fracturing on a reservoir scale in 2D, *J. Petrol. Sci. Eng.*, *77*, 274–285.

Witherspoon, P. A, J. Wang, K. Iwai, and J. Gale (1980), Validity of cubic law for fluid flow in a deformable rock fracture, *Water Resour. Res.*, *16*(6), 1016–1024.

Erratum